Buckling Testing and Analysis of Honeycomb Sandwich Panel Arc Segments of a Full-Scale Fairing Barrel

Part 3: 8-Ply Out-of-Autoclave Facesheets

Evan J. Pineda and David E. Myers
Glenn Research Center, Cleveland, Ohio

Daniel N. Kosareo
Vantage Partners, LLC, Brook Park, Ohio

Sotiris Kellas
Langley Research Center, Hampton, Virginia

NASA STI Program . . . in Profile

Since its founding, NASA has been dedicated to the advancement of aeronautics and space science. The NASA Scientific and Technical Information (STI) program plays a key part in helping NASA maintain this important role.

The NASA STI Program operates under the auspices of the Agency Chief Information Officer. It collects, organizes, provides for archiving, and disseminates NASA's STI. The NASA STI program provides access to the NASA Aeronautics and Space Database and its public interface, the NASA Technical Reports Server, thus providing one of the largest collections of aeronautical and space science STI in the world. Results are published in both non-NASA channels and by NASA in the NASA STI Report Series, which includes the following report types:

- TECHNICAL PUBLICATION. Reports of completed research or a major significant phase of research that present the results of NASA programs and include extensive data or theoretical analysis. Includes compilations of significant scientific and technical data and information deemed to be of continuing reference value. NASA counterpart of peer-reviewed formal professional papers but has less stringent limitations on manuscript length and extent of graphic presentations.

- TECHNICAL MEMORANDUM. Scientific and technical findings that are preliminary or of specialized interest, e.g., quick release reports, working papers, and bibliographies that contain minimal annotation. Does not contain extensive analysis.

- CONTRACTOR REPORT. Scientific and technical findings by NASA-sponsored contractors and grantees.

- CONFERENCE PUBLICATION. Collected papers from scientific and technical conferences, symposia, seminars, or other meetings sponsored or cosponsored by NASA.

- SPECIAL PUBLICATION. Scientific, technical, or historical information from NASA programs, projects, and missions, often concerned with subjects having substantial public interest.

- TECHNICAL TRANSLATION. English-language translations of foreign scientific and technical material pertinent to NASA's mission.

Specialized services also include creating custom thesauri, building customized databases, organizing and publishing research results.

For more information about the NASA STI program, see the following:

- Access the NASA STI program home page at *http://www.sti.nasa.gov*

- E-mail your question to *help@sti.nasa.gov*

- Fax your question to the NASA STI Information Desk at 443–757–5803

- Phone the NASA STI Information Desk at 443–757–5802

- Write to:
  STI Information Desk
  NASA Center for AeroSpace Information
  7115 Standard Drive
  Hanover, MD 21076–1320

Buckling Testing and Analysis of Honeycomb Sandwich Panel Arc Segments of a Full-Scale Fairing Barrel
Part 3: 8-Ply Out-of-Autoclave Facesheets

Evan J. Pineda and David E. Myers
Glenn Research Center, Cleveland, Ohio

Daniel N. Kosareo
Vantage Partners, LLC, Brook Park, Ohio

Sotiris Kellas
Langley Research Center, Hampton, Virginia

National Aeronautics and
Space Administration

Glenn Research Center
Cleveland, Ohio 44135

June 2014

Level of Review: This material has been technically reviewed by technical management.

Buckling Testing and Analysis of Honeycomb Sandwich Panel Arc Segments of a Full-Scale Fairing Barrel
Part 3: 8-Ply Out-of-Autoclave Facesheets

Evan J. Pineda and David E. Myers
National Aeronautics and Space Administration
Glenn Research Center
Cleveland, Ohio 44135

Daniel N. Kosareo
Vantage Partners, LLC
Brook Park, Ohio 44142

Sotiris Kellas
National Aeronautics and Space Administration
Langley Research Center
Hampton, Virginia 23681–2199

Abstract

Four honeycomb sandwich panels, representing 1/16th arc segments of a 10 m diameter barrel section of the heavy lift launch vehicle, were manufactured under the NASA Composites for Exploration program and the NASA Constellation Ares V program. Two configurations were chosen for the panels: 6-ply facesheets with 1.125 in. honeycomb core and 8-ply facesheets with 1.000 in. honeycomb core. Additionally, two separate carbon fiber/epoxy material systems were chosen for the facesheets: in-autoclave IM7/977-3 and out-of-autoclave T40-800B/5320-1. Smaller 3- by 5-ft panels were cut from the 1/16th barrel sections. These panels were tested under compressive loading at the NASA Langley Research Center. Furthermore, linear eigenvalue and geometrically nonlinear finite element analyses were performed to predict the compressive response of the 3- by 5-ft panels. This manuscript summarizes the experimental and analytical modeling efforts pertaining to the panel composed of 8-ply, T40-800B/5320-1 facesheets (referred to as Panel C). To improve the robustness of the geometrically nonlinear finite element model, measured surface imperfections were included in the geometry of the model. Both the linear and nonlinear, two-dimensional (2-D) and three-dimensional (3-D), models yield good qualitative and quantitative predictions. Additionally, it was predicted correctly that the panel would fail in buckling prior to failing in strength.

1.0 Introduction

Two manufacturing demonstration honeycomb sandwich panels (1/16th arc segments of the 10 m diameter cylinder) were fabricated under the NASA Composites for Exploration (CoEx) program and two under the NASA Constellation Ares V program. All four panels were manufactured by Hitco Carbon Composites. Two distinct configurations were chosen for the panels. The first configuration, fabricated under the CoEx program, was composed of 8-ply facesheets with a [45°/90°/-45°/0°]$_s$ lay-up and 1.000 in. aluminum (Al) honeycomb core. The second configuration, fabricated under the Constellation Ares V program, consisted of 6-ply facesheets with a [60°/-60°/0°]$_s$ stacking sequence and a 1.125 in. Al honeycomb core. In addition to the two configurations, two different carbon fiber/epoxy facesheet material systems were chosen for the panels: in-autoclave (IA) IM7/977-3 and out-of-autoclave (OOA) T40-800B/5320-1. It should also be noted that the honeycomb used in the 8-ply panels was machined to

match the curvature of the panel while the honeycomb used in the 6-ply panels was flat. Additionally, in each panel, an adhesive splice joint was used to join discontinuous sections of the honeycomb core.

Following delivery to NASA Langley Research Center, non-destructive evaluation (NDE) inspection (including ultrasonic testing and flash thermography) was performed on the full manufacturing demonstration panel. The results of the NDE guided the decision on where to cut 36 in. wide by 62 in. long sections for edgewise compression buckling tests. Following removal of the 36- by 62-in. panels from the manufacturing demo and after, the panels were re-inspected using infrared (IR) thermography to ensure that no damage had occurred. In preparation for testing, the load introduction ends of the panels were potted in 1.0 in thick Al end plates. The purpose of the end plates was to stabilize the facesheets and prevent local crushing, thus generating a predictable and repeatable end condition. As such, the panels are referred to as 3- by 5-ft according to the acreage dimensions of the test panels. Preliminary finite element analysis (FEA) indicated that no additional reinforcement was needed at the load introduction ends of the panels. A summary of the five 3- by 5-ft panels that were tested is given in Table 1.

TABLE 1.—DETAILS OF FIVE 5-ft TALL BY 3-ft WIDE PANELS CUT FROM 1/16TH ARC
SEGMENTS OF 10.0 m BARREL SECTION THAT WERE LOADED UNTIL BUCKLING
[Composite Manufacturing Demonstration Panel (CMDP) and Manufacturing Test Panel (MTP)]

3- by 5-ft panel I.D.	1/16th arc segment panel I.D.	Facesheet material	Facesheet lay-up	Core thickness, in.
Panel A	8000-CMDP	IM7/977-3 (IA)	[45°/90°/-45°/0°]$_s$	1.000 (curved)
Panel B-1	MTP-6003	IM7/977-3 (IA)	[60°/-60°/0°]$_S$	1.125 (flat)
Panel B-2	MTP-6000	IM7/977-3 (IA)	[60°/-60°/0°]$_S$	1.125 (flat)
Panel C	8010-CMDP	T40-800B/5320-1 (OOA)	[45°/90°/-45°/0°]$_s$	1.000 (curved)
Panel D	MTP-6010	T40-800B/5320-1 (OOA)	[60°/-60°/0°]$_S$	1.125 (flat)

The current document provides details specifically pertaining to Panel C, which consisted of 8-ply facesheets composed of OOA T40-800B/5320-1 and a 1.000 in. honeycomb core. Similar, separate documents have been prepared for Panels A, B, and D. The remaining subsections of Section 1.0 summarize the experimental and modeling objectives pertaining to all four panels. Section 2.0 provides details on Panel C. Section 3.0 describes several approaches that were used to predict the buckling load of Panel C. The experimental and numerical results are presented in Section 4.0. Finally, results from 3-D analyses are presented in Section 5.0. Previous parametric studies were performed on similar panels to determine the sensitivity of the buckling load of the panels to varying degrees of imperfections including as manufactured geometry, fiber angle misalignment, and loading eccentricity (Myers et al., 2013; Pineda et al., 2013). These sensitivity studies were not performed for Panel C.

1.1   Test Objectives

The primary objective of the test is to measure the maximum compressive load carrying capability (buckling load) of each 3 ft wide by 5 ft long panel and to provide data for analysis correlation and validation. A secondary objective is to study the effect of manufacturing defects on the deformation and buckling load.

1.2   Test Success Criteria

The test will be considered successful if each of the following criteria are met:

1. All critical instrumentation is fully operational during the test
2. The loads are applied in a uniform and controlled manner
3. Maximum attained load and all associated data are recorded and saved in the desired format

1.3 Modeling Objectives

The primary modeling objective is to predict the global buckling load and structural response of each 3-ft wide by 5-ft long panel as accurately as possible using standard, commercially available, analysis tools. A linear eigenvalue baseline, obtained from the finite element method (FEM), will be compared to the experiment. More sophisticated, progressive collapse analyses, incorporating non-linear geometric effects and the measured geometric imperfections of the panel surfaces, will be executed in an attempt to improve the baseline numerical (FEM) prediction. Additionally, linear strength analyses will be performed to ensure that predicted buckling occurs before expected strength failure.

1.4 Modeling Success Criteria

The modeling will be considered successful if each of the following criteria are met:

1. The buckling load is predicted within 20 percent
2. The buckling mode/direction and location is predicted accurately
3. Local strain fields correlate well qualitatively with visual imaging data measured during the experiment

2.0 1/16th Panel Description

The 1/16th fabrication demo panel was constructed on a concave composite tool (5 m radius of curvature) using an automated tape laying process. The pre-impregnated (prepreg) tape was composed of unidirectional fibers and was 6 in. wide. The prepreg contained T40-800B fibers and 5320-1 epoxy. The stacking sequence of the facesheets was [45°/90°/-45°/0°]$_s$. The facesheets were bonded to the 1 in. thick Al core using FM 300 film adhesive, 0.08 lb/ft^2. The Al honeycomb core was curved, via machining, to match the radius of the tool. The Al core was Alcore PAA-CORE 5052, 0.000700 in thick with 0.1250 in cell size, and a density of 3.1 pcf. An adhesive splice was needed to join discontinuous sections of the core because the 1/16th barrel section panel dimensions exceeded the size of the pre-manufactured core. A Hysol 9396.6 foaming adhesive was used to fill the gap between the two pieces of Al core. The facesheets and core adhesive were co-cured OOA. The manufacturing demonstration 1/16th arc segment (of a 5 m outside radius cylinder) panel is shown in Figure 1.

Figure 1.—Cured 1/16th arc segment panel and the tool it was molded on.

2.1   Test Specimen Description

One 36 in. wide by 62 in. long test specimen was machined from the manufacturing demo panel following non-destructive examination. The end plates were 1.0 in. thick Al plates and had a slot in the shape of the specimens cross section machined in the center. The slot width and length were such that, when centered, the specimen had a clearance of 0.5 in. around the perimeter. After the specimen-end was centered in the slot and squared, it was potted with "UNISORB" V-100 epoxy grout. When both ends were potted and following cure, specimen ends were machined flat and parallel to within ±0.0025 in. A photograph of the test specimen with potted ends is shown in Figure 2. The potted dimensions of the 5320-1 panel are shown in Figure 3. In addition to the overall dimensions, Figure 3 shows the relative position of the core splice with respect to the panel ends. For complete details on the CoEx experimental efforts, the reader is referred to Kellas, et al. (2012).
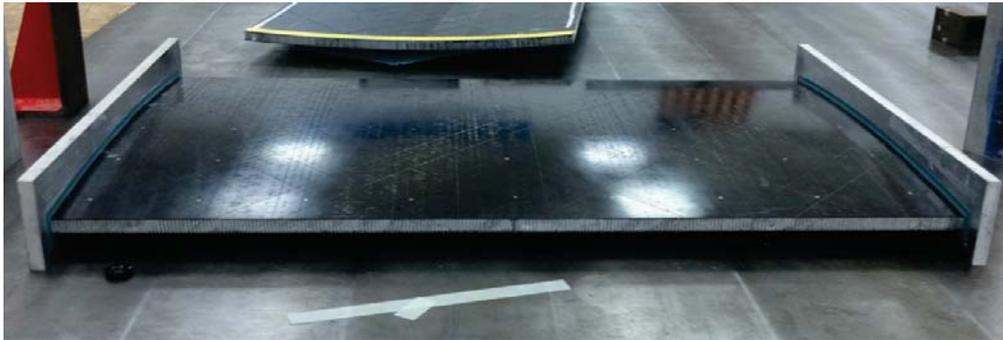
Figure 2.—Test panel with potted Al end plates.
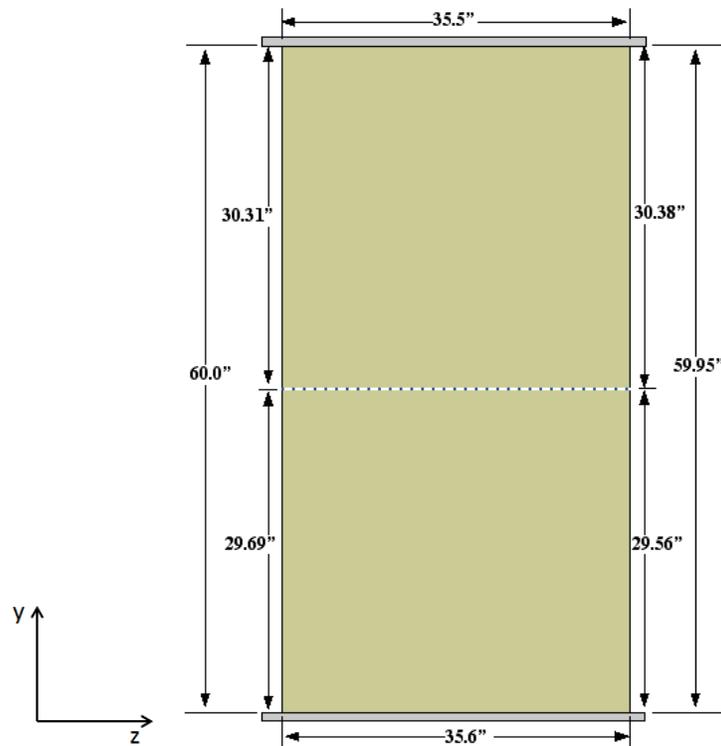
Figure 3.—Potted specimen dimensions. Note: outside surfaces of Al end plates were machined flat and parallel. Position of core splice shown relative to inside surface of Al end plates.
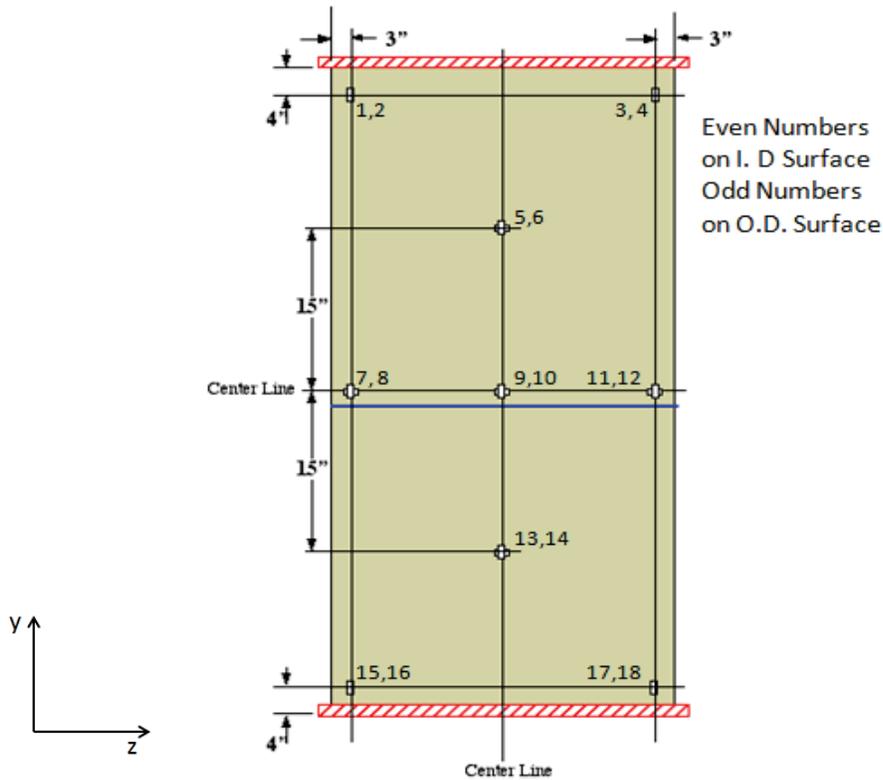
Figure 4.—Panel geometry and strain gage location/nomenclature.

Once potted, strain gages were affixed to the inner diameter (I.D. or IML) and outer diameter (O.D. or OML) surfaces of the panel, as shown in Figure 4. The even numbered gages were located on the I.D. while the odd numbered gages were located on the O.D. These gages were monitored and the strains were recorded during loading of the panel. The panel was tested at the NASA Langley Research Center (LaRC) in a servo-hydraulic test frame. The panel was secured between two loading platens, with the bottom loading platen being fixed and the top platen allowed to move in the y-direction. The panel was loaded in compression until buckling failure occurred. Additional instrumentation included three direct-current displacement transducers (DCDTs) used to measure the global, axial deformation of the panel, and a load cell attached to the load platen to measure the applied load. Finally, the panels were painted using a speckle pattern for photogrammetric measurements. Visual image correlation (VIC) was employed to obtain full-field strain measurements during the test as well as high speed video.

3.0   Finite Element Analysis Description

Pre-test predictions of the buckling load for Panel C were determined using commercially available FEM software packages: MSC/NASTRAN, Abaqus, and ANSYS. Figure 5 shows the test panel geometry used in the FEM models. The panel was modeled as 60.00 in. tall (section between the Al end plates) and 35.55 in. along the arc (35.5 in. along the chord) using 2-D layered shell elements. The 1.0 in. sections of the panel on the top and bottom that were supported in the potting material were not modeled. The element size was 1.0- by 1.0-in., and the model was comprised of 2257 nodes and 2160 elements. No shell element offsets were used, so the 2D panel geometry represents the panel centerline. All three displacements and all three rotations were fixed along the bottom edge of the panel. The same boundary condition was applied to the top edge, except a displacement was applied in the negative y-direction.

The stacking sequence of the facesheets was [45°/90°/-45°/0°]s with 0.0053 in. plies. The T40-800B/5320-1 elastic properties and allowables (used in strength analysis) were obtained from the Orion materials database, and are not shown as they are ITAR restricted (Lockheed Martin, 2010). The Al honeycomb properties were obtained from the database included with the commercially available structural sizing software, HyperSizer, and are presented in Table 2. The in-plane normal and shear stiffnesses were reduced from 75.0 ksi to 1.00×10^{-7} ksi since in-plane load carrying capability of the honeycomb is typically neglected in honeycomb sandwich panel analysis.
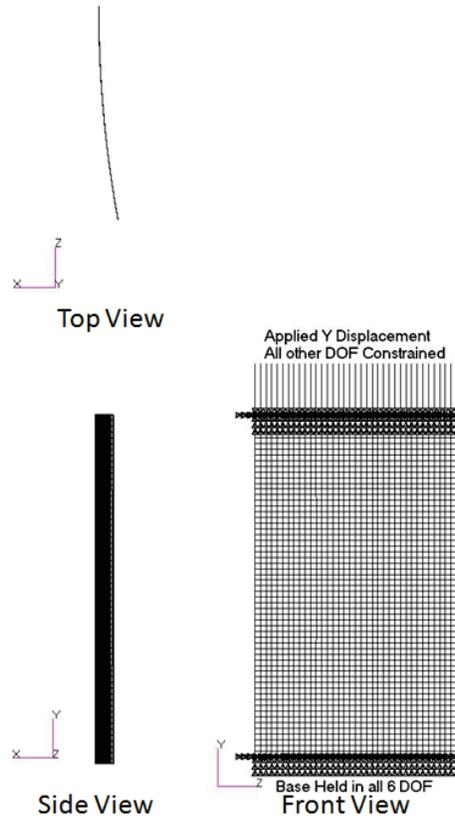
Figure 5.—Panel geometry with boundary conditions.

TABLE 2.—AL HONEYCOMB MATERIAL
PROPERTIES, 3.1 pcf, 1/8 in.-5052-0.0007

E_1, ksi	1.00×10^{-7}
E_2, ksi	1.00×10^{-7}
ν_{12}	0.333
G_{12}, ksi	1.00×10^{-7}
G_{1Z}, ksi	45.0
G_{2z}, ksi	22.0
ρ, pcf	3.10
F_{t1}, ksi	0.200
F_{c1}, ksi	0.200
F_{t2}, ksi	0.200
F_{c2}, ksi	0.200
F_{s12}, ksi	0.090

To arrive at a baseline buckling failure prediction, a linear eigenvalue buckling analysis (Sol 105) was performed in MSC/NASTRAN. This preliminary analysis was executed for two reasons. First, the analysis provides a reasonable estimate of what the non-linear analysis should predict as the panel buckling load with an efficient, quick turnaround. Second, this is the typical method of calculating buckling loads for flight structures, and it is informative to compare the results to the experimental buckling load and the buckling loads obtained from higher-fidelity models.

In addition, to improve numerical predictions, it was also pertinent to predict which direction (towards the I.D. or O.D.) the panel would buckle as a DCDT was to be placed to measure the out-of plane displacement of the panel and severe displacement in the unexpected direction would damage the gage. The eigenvectors obtained from a linear eigenvalue analysis are in an arbitrary direction and do not indicate the direction the panel would buckle. Therefore, geometrically non-linear static analyses were performed in MSC/NASTRAN (Sol 106), Abaqus, and ANSYS to arrive at a more accurate buckling load and determine the direction of buckling correctly.

Hause et al. (1998, 2000), Hilburger et al. (2001), Hilburger and Starnes, Jr. (2002), Lynch et al. (2004), Schultz and Nemeth (2010) have shown that FEM simulations of progressive collapse incorporating geometric non-linearities are extremely sensitive to the geometric imperfections in the panel. Thus, it was desired to use some measure of the actual imperfections of the panel and include them in the model. Preliminary photogrammetry data of the panel showed that the bag side (I.D.) surface contained some initial imperfections that were biased towards the I.D. On the O.D., or the tool side, the surface imperfections were sinusoidal in nature. Herein, these surface imperfections are referred to as the bow shape of the panel. In the progressive collapse analyses, the bow data from the bag side of the panel was used to incorporate geometric imperfections into the model. Figure 6 shows the imperfection, or bow, data measured vertically from the top of the panel to the bottom of the panel at the horizontal center. The raw photogrammetry data was first rotated such that both the top and bottom had an out-of-plane bow displacement of 0.0 in. The data was then scaled (60 in./total height of photogrammetry data) so that it covered the full 60 in. of the panel. These two modifications resulted in the curve labeled "Laser Track" in Figure 6. The photogrammetry data was interpolated to arrive at the approximated bow shape used in the NASTRAN model, labeled "NASTRAN Bow" in Figure 6. The approximated bow geometry was then swept along an arc of radius 198.0 in. and 10.272°, providing a uniform tangential panel cross section. Realistically, the cross section of the panel varies in the circumferential direction, but it was assumed that the imperfect, but uniform, cross section used in the numerical model is sufficient to capture the primary effects of the geometric imperfections in the panel. Similarly, the imperfection geometry was represented within Abaqus using fewer data points, labeled "Abaqus Bow" in Figure 6.

Finally a linear static solution in MSC/NASTRAN (Sol 101) was executed to determine the strength margins of safety at the time of onset of buckling. A similar analysis was performed in HyperSizer. These results were used to determine whether the failure of the panel was stiffness critical (buckling) or strength critical (local facesheet or core failure).
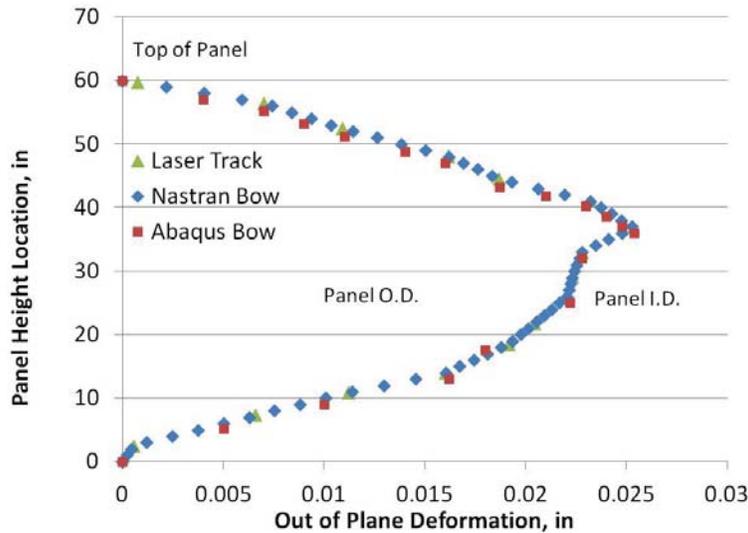
Figure 6.—Imperfection, or bow, data from the bag side (I.D.) of the panel. Data were taken vertically along the height of the panel, in the horizontal center of the panel.
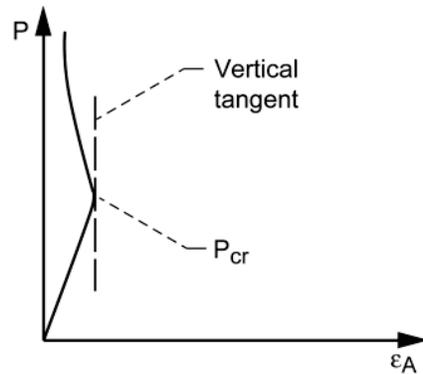

Figure 7.—Method for determining buckling load from Singer, et al. (1998).

4.0   Test and Analysis Comparison

To determine the panel buckling load a method from Singer, et al. (1998), shown in Figure 7, was used. This method utilizes global load versus local strain gage data (axial strain) to mark the onset of buckling. In Figure 7, a vertical tangent line intersects the load-strain curve at a local strain where the local strain increment reverses which is designated the local buckling strain. The load corresponding to that local strain is designated the buckling load. It should be noted that the buckling strain, and hence buckling load, can only be determined at monitored locations and therefore can actually be lower than the lowest measured value. Thus, the postulated buckling load is somewhat subjective and based upon the location where the strains are being monitored for reversal. Test data for Gages 7 and 8 exhibited strain reversal at the lowest applied edge load. This load, 71,613 lb will be considered the buckling load, and the numerical buckling loads will be determined from the global load versus local strain plots obtained from points on the models corresponding to these gage locations.
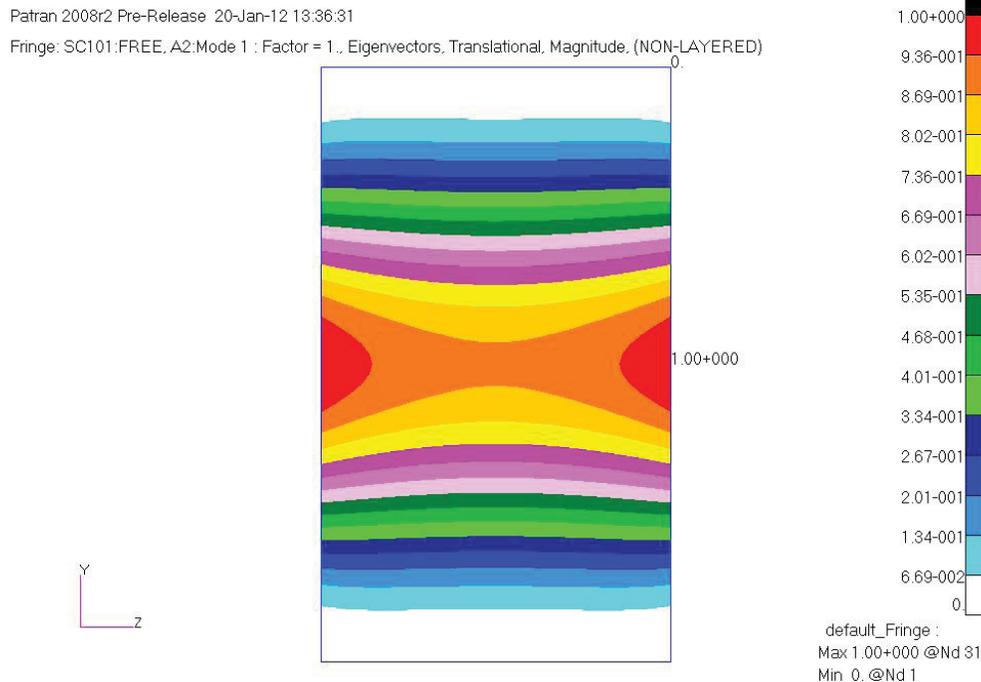
Figure 8..—Euler eigenvector buckling plot obtained from MSC/NASTRAN.

4.1 Linear Buckling Analysis

A linear buckling analysis was performed using NASTRAN Sol 105. Figure 8 shows the eigenvector plot when -0.198 in. was applied to the edge. The corresponding reaction load was 82,318 lb. Thus, the linear eigenvalue solution predicted a buckling load 14.9 percent higher than the test results. As mentioned before, the eigenvectors do not indicate the direction of buckling in a panel where there is a preferred direction, such as a curved panel.

4.2 Non-Linear Buckling Analysis

To obtain a more accurate prediction of the buckling load, a pre-test, geometrically non-linear analysis was executed using MSC/NASTRAN Sol 106. For verification, several additional analyses were completed, including static nonlinear ANSYS, and static nonlinear Abaqus. Note that the ANSYS model included both the approximated imperfection geometry presented in Figure 6 and was seeded using the mode shapes from a preliminary, linear eigenvalue buckling analysis. For complete details on the ANSYS analysis, please refer to Section 4.1. Table 3 summarizes details of the various analysis tools that were used to predict the buckling load of the panel. Figure 9 shows the load-deflection curves for all analyses as well as the experiment. The figure shows that all four analyses closely match the test data.

TABLE 3.—SUMMARY OF ANALYSIS TOOLS USED TO PREDICT BUCKLING RESPONSE OF SANDWICH PANEL

| Software	Solution	Description	Imperfection Seeding
MSC/NASTRAN	105	Linear eigenvalue solution	Approximated bow
MSC/NASTRAN	106	Static solution with nonlinear geometry	Approximated bow
Abaqus	Static, NLGEOM	Static solution with nonlinear geometry	Approximated bow
ANSYS	Static, NLGEOM	Static solution with load increments and nonlinear geometry	Mode shapes and approximated bow
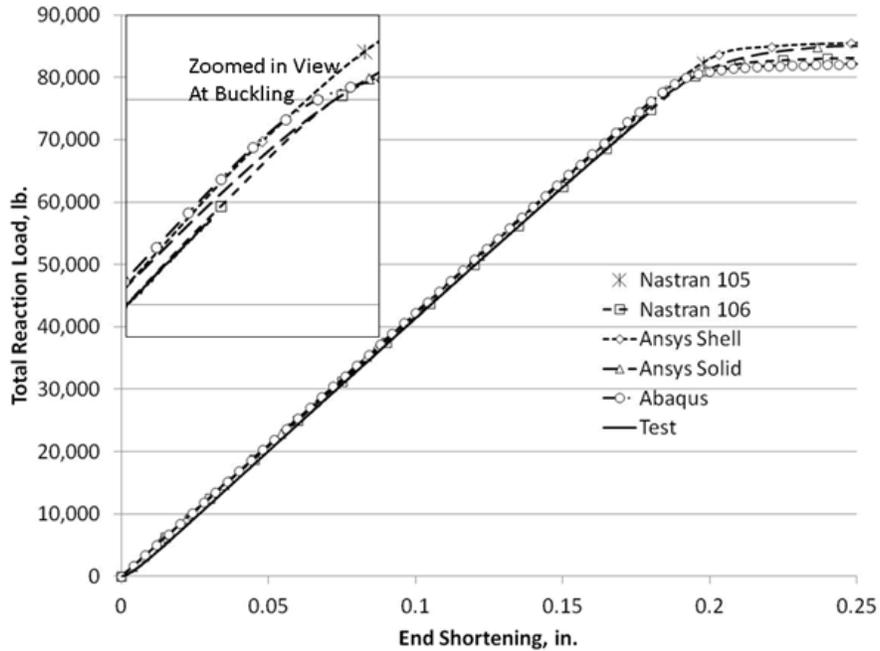
Figure 9.—Total reaction load versus end shortening for all analyses.
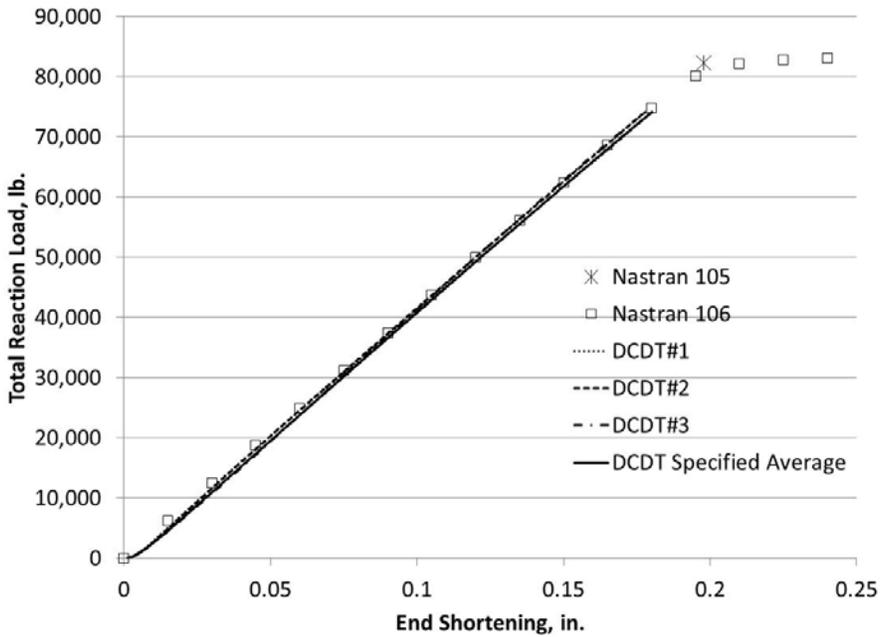

Figure 10. DCDT end shortening versus total reaction load.

In all the analyses the linear pre-buckling panel stiffness was nearly the same. However, the stiffness obtained from the analyses was slightly higher than the test stiffness. Figure 10 shows the measurements of all three DCDTs that were affixed to the panel during loading. DCDT#1 aligned almost perfectly with the NASTRAN Sol 106 results (the most over-predicted results) while DCDT#2 and #3 showed lower stiffnesses, yielding an average measurement that produces a lower stiffness than the analytical predictions. Additionally, there is some initial non-linearity in the DCDT results. This indicates that there

is some settling due to contact as the panel is initially loaded. The slopes of the "NASTRAN SOL 106," DCDT#1," "DCDT#2," "DCDT#3," and "DCDT Specified Average" curves are presented in Table 4 at an end shortening of 0.1 in. (to eliminate settling). The analytical predicted stiffness was slightly above all the DCDT#1 readings, but below DCDT#2, DCDT#3 and the average. However, this discrepancy is minimal.

For simplification, only analytical results obtained from MSC/NASTRAN will be presented in the remainder of this section (Section 4.2). Figure 11 shows the out-of-plane displacement contour plot and deformed shape obtained from analysis, at an applied edge displacement of -0.25 in., well into the post-buckled regime. This plot displays that panel buckling was predicted towards the I.D, which is consistent with the buckling direction observed in the experiment.

TABLE 4.—TANGENT SLOPES OF CURVES IN
FIGURE 10 AT AN END SHORTENING OF 0.1 in.

Curve	Slope
NASTRAN SOL 106, kips/in.	416.1
DCDT#1, kips/in.	415.8
DCDT#2, kips/in.	423.8
DCDT#3, kips/in.	435.1
DCDT specified average, kips/in.	424.3
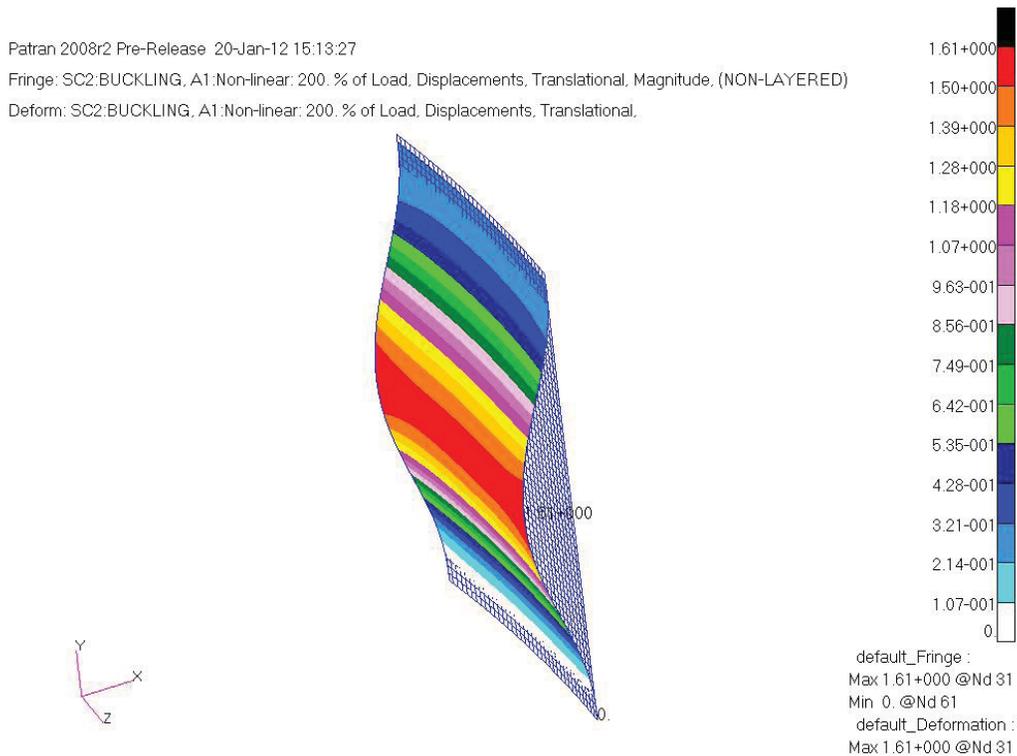
Figure 11. Panel displacement plot for -0.25 in. applied edge displacement.

The buckling load determined using the highest strain located at the vertical center of the panel near the edges was 74,493 lb. Loads corresponding to all strain gage locations are tabulated with the experimental values in Table 5. Figure 12 and Figure 13 show that, in the corner, the axial O.D. panel strain goes into compression up to the onset of buckling, after which the strain increment reverses and the axial strain is alleviated as the load increases during post-buckling. This local behavior (observed both experimentally and numerically) is consistent as the panel buckled towards the I.D. Note that, since the major curvature of the panel is biased towards the O.D., the analysis would predict buckling towards the O.D. if no geometric imperfections (bow) were introduced into the model. Figure 14 shows the strain gage measurements at a panel inflection point at the ¾ panel length location. Figure 15-Figure 17 shows that at the horizontal center of the panel, the I.D. panel strain goes into compression up to buckling and then starts to reverse as the load increases during post-buckling. The results from Figure 18 the lower inflection or ¼ length location, match the results from Figure 14 while the results from Figure 19 and Figure 20 match the results from Figure 12 and Figure 13, respectively. The error in the nonlinear analysis ranges from 3.9 percent (Table 5), which was a significant improvement over the linear analysis.

TABLE 5.—APPROXIMATE TEST AND ANALYSIS PREDICTION BUCKLING LOADS
[See Figure 4 for gage locations on panel.]

Gage	Test, lb	Analysis, lb	Error, %
1,2	74,169	76,128	2.6
3,4	74,169	76,128	2.6
7,8	71,613	74,493	3.9
9,10	74,169	76,128	2.6
11,12	71,819	74,493	3.6
15,16	74,169	76,128	2.6
17,18	74,169	76,128	2.6
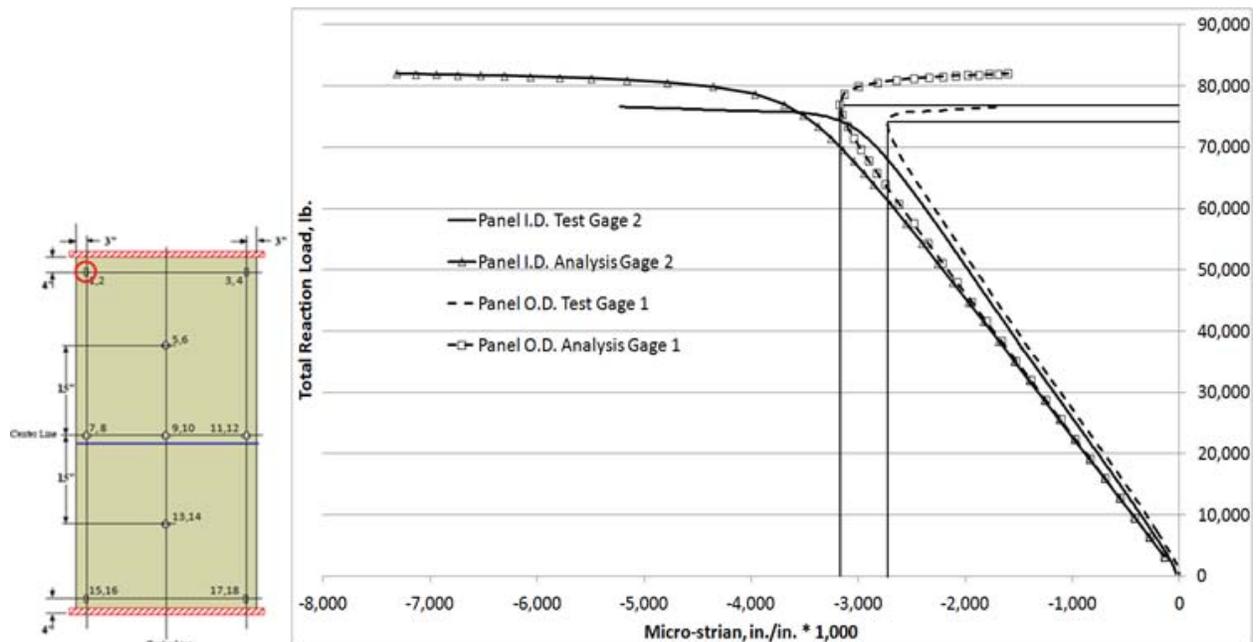
Figure 12.—Load/strain plot for gages 1 and 2, upper left corner of panel, even nos. on I.D. (see Figure 4). Analysis obtained from MSC/NASTRAN, Sol 106.
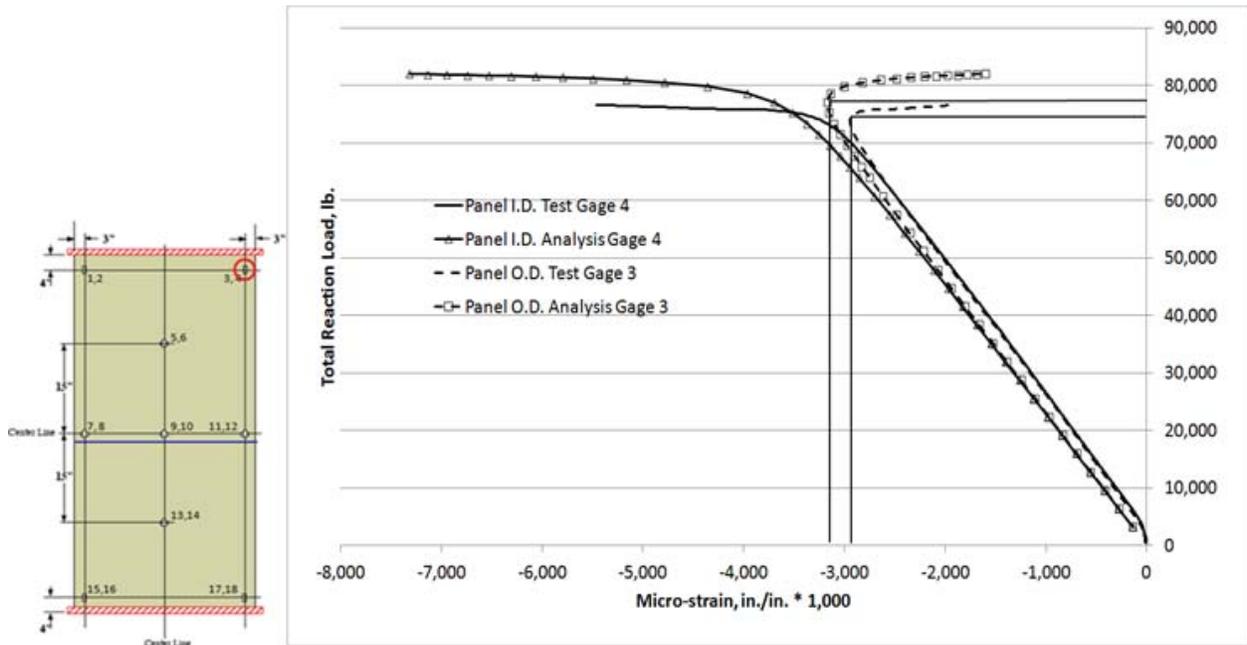
Figure 13.—Load/strain plot for gages 3 and 4, upper right corner of panel, even nos. on I.D. (see Figure 4). Analysis obtained from MSC/NASTRAN, Sol 106.
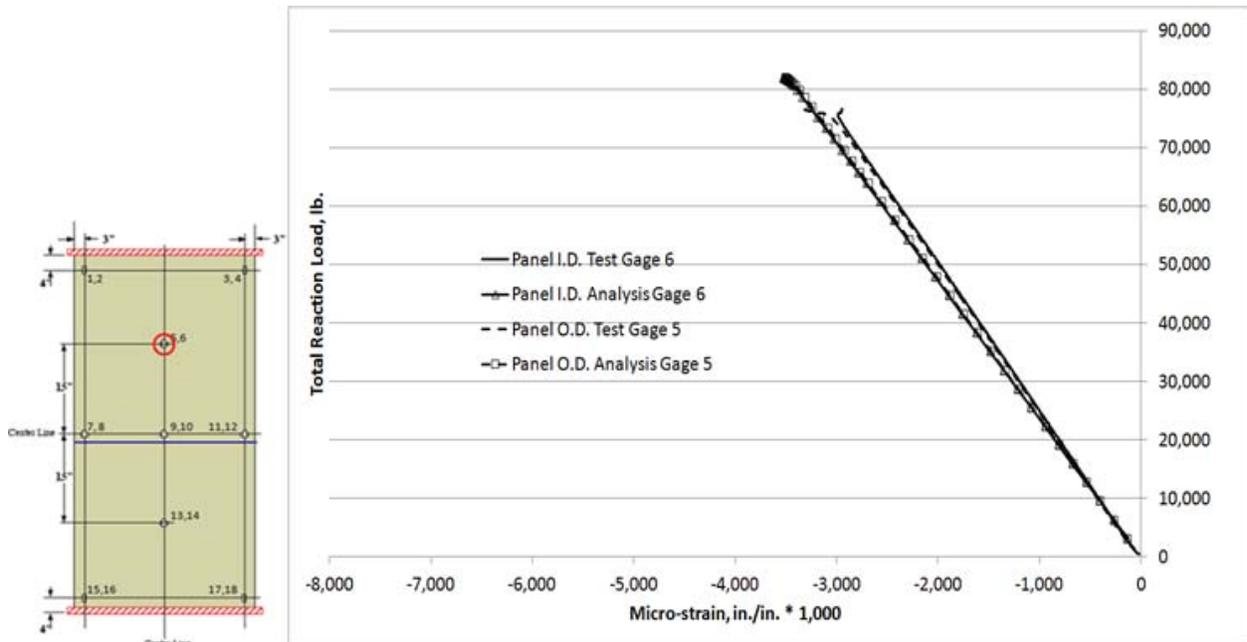

Figure 14.—Load/strain plot for gages 5 and 6, at panel inflection point, ¾, even nos. on I.D.(see Figure 4). Analysis obtained from MSC/NASTRAN, Sol 106.
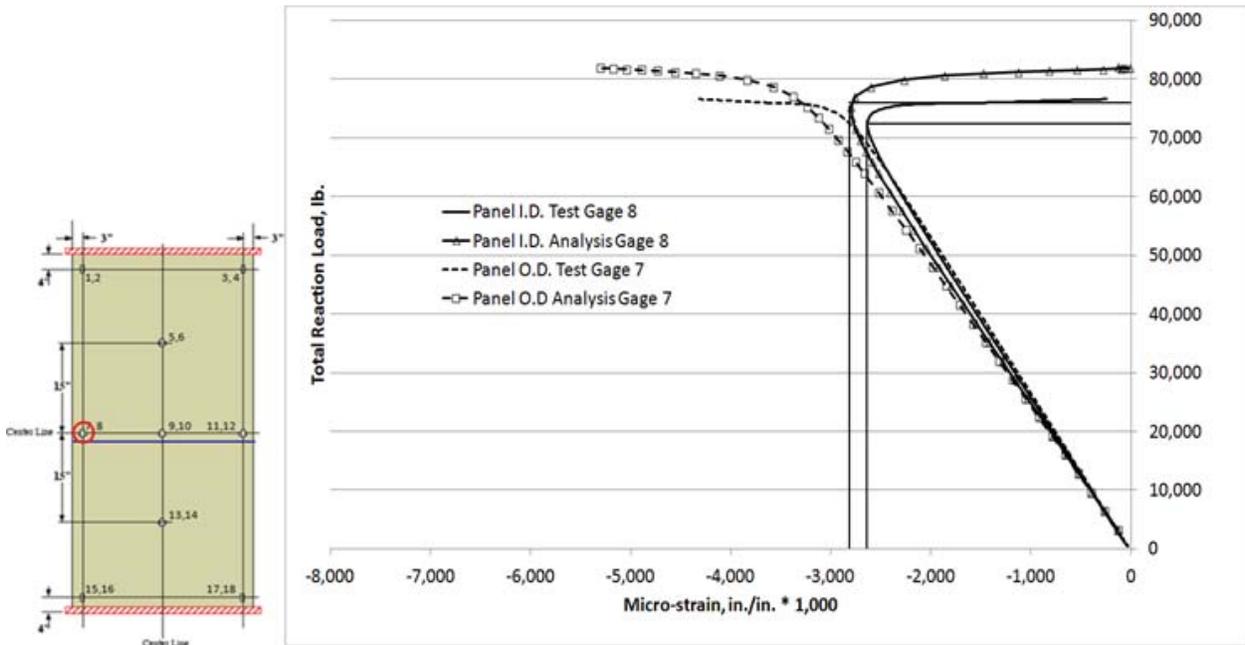
Figure 15.—Load/strain plot for gages 7 and 8, at horizontal left side, even nos. on I.D. (see Figure 4). Analysis obtained from MSC/NASTRAN, Sol 106.
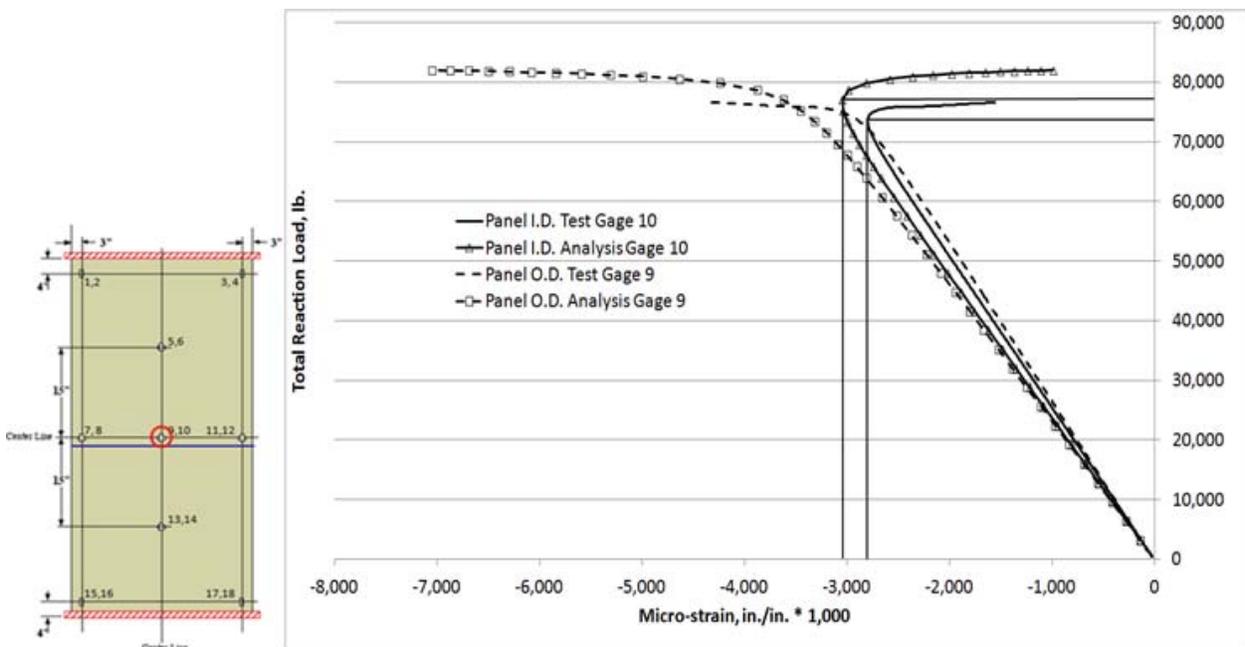

Figure 16.—Load/strain plot for gages 9 and 10, center of panel, even nos. on I.D. (see Figure 4). Analysis obtained from MSC/NASTRAN, Sol 106.
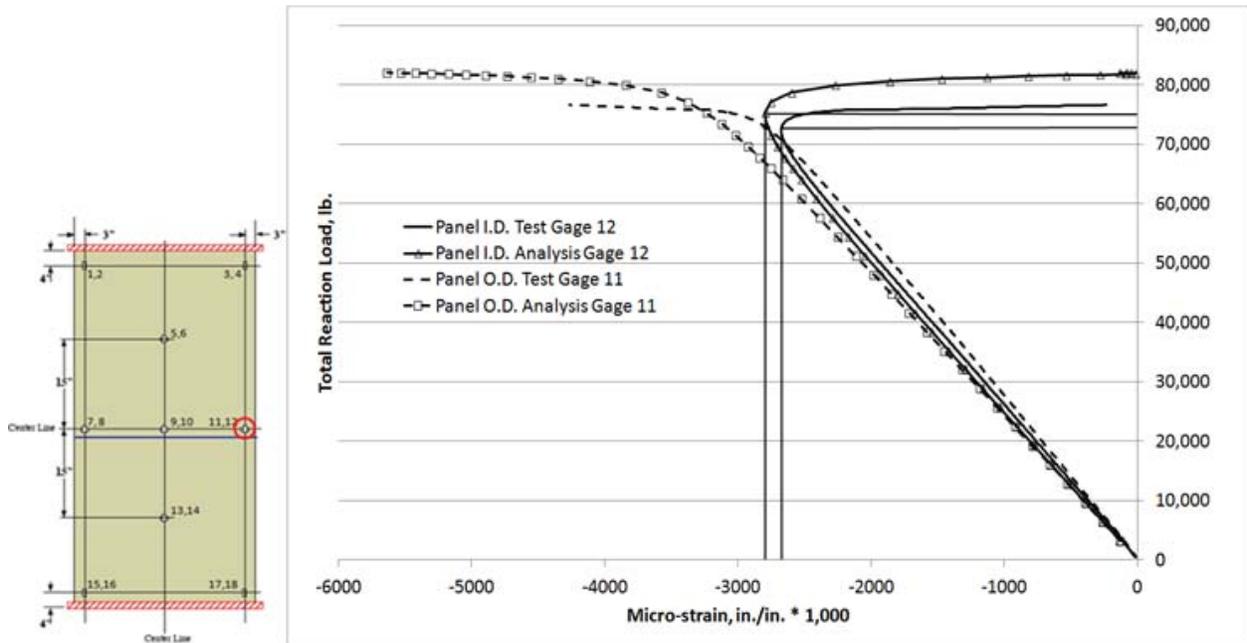
Figure 17.—Load/strain plot for gages 11 and 12, center of panel, right side, even nos. on I.D. (see Figure 4). Analysis obtained from MSC/NASTRAN, Sol 106.
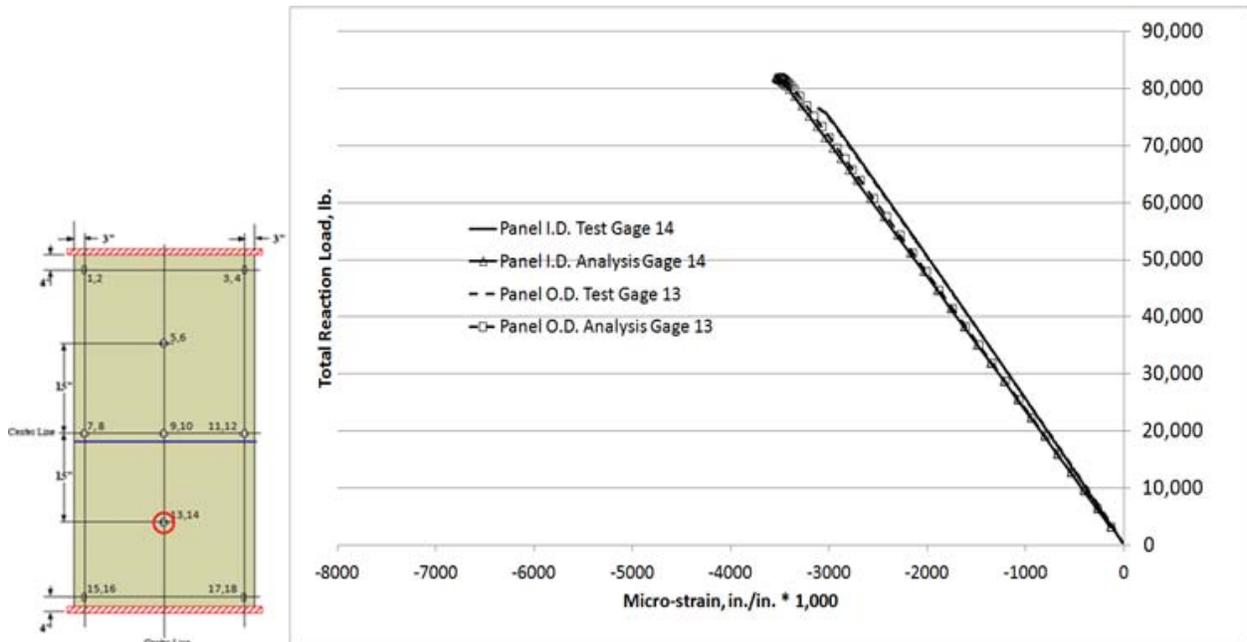
Figure 18.—Load/strain plot for gages 13 and 14, centerline of panel, ¼ length, even nos. on I.D. (see Figure 4). Analysis obtained from MSC/NASTRAN, Sol 106.
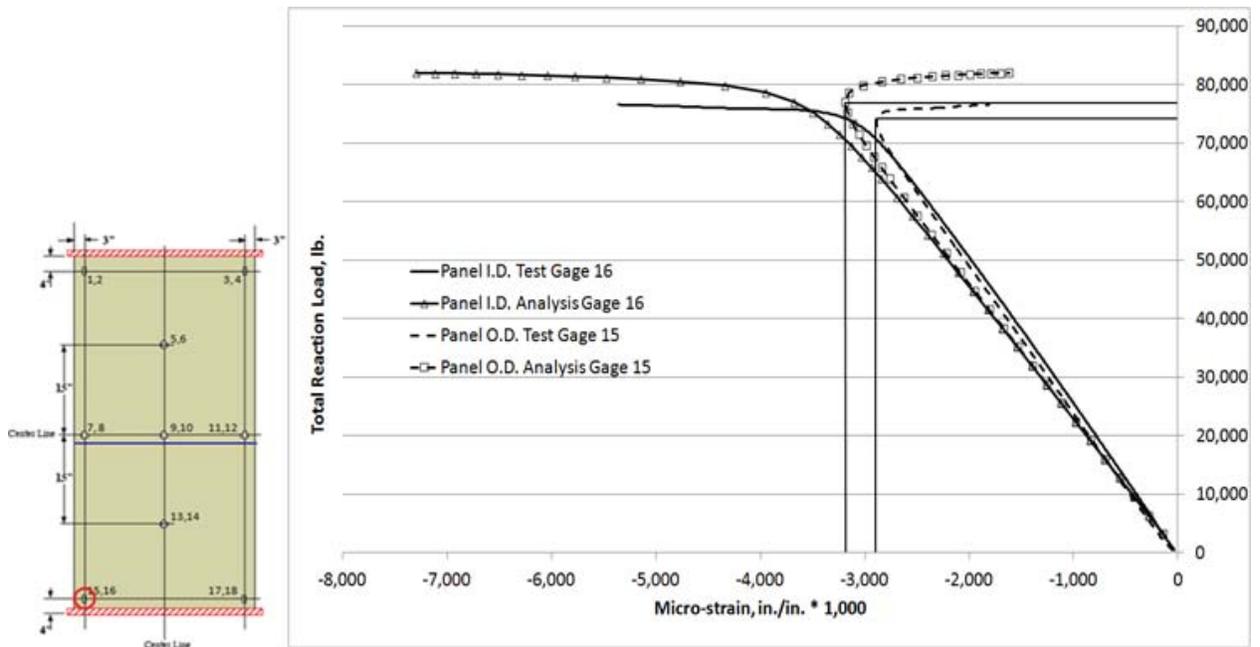
Figure 19.—Load/strain plot for gages 15 and 16, lower left of panel, even nos. on I.D. (see Figure 4). Analysis obtained from MSC/NASTRAN, Sol 106.
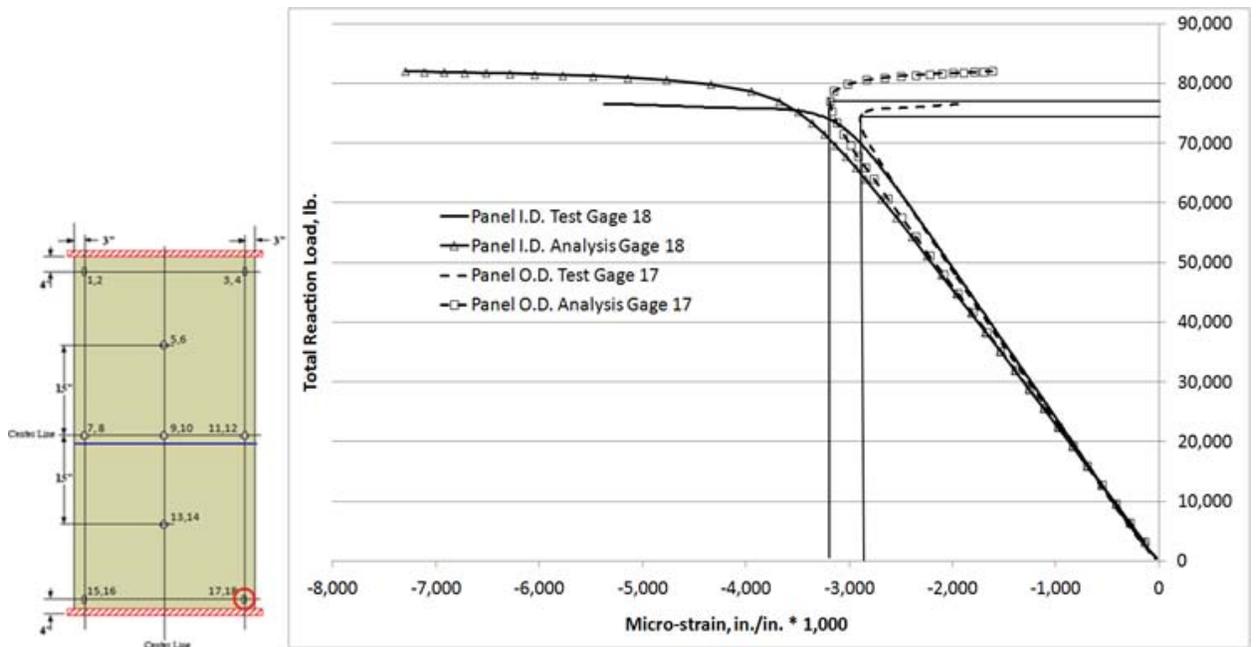
Figure 20.—Load/strain plot for gages 17and 18, lower right, even nos. on I.D. (see Figure 4). Analysis obtained from MSC/NASTRAN, Sol 106.

Figure 21 shows that the post-buckled, out-of plane, displacement compared well qualitatively with the analytical predictions. Since shell elements were used in the analysis, the nodal displacements do not vary on the O.D. and I.D. surfaces, whereas, the test results showed some slight variation in displacement for the I.D. and O.D. surfaces due to the finite width of the panel. For the I.D. surface, Figure 22 shows that the minimum principal strain also compared well. For the O.D. surface, Figure 23 show that the post-buckled, minimum principal strain analytical predictions, no test corresponding test results were available. However, based on previous results for other material systems (Myers et al., 2013; Pineda et al., 2013), it is expected that these results are qualitatively accurate. Figure 24 shows the maximum principal strain comparison for the I.D., and Figure 25 shows just the analysis results for the O.D. The comparison in Figure 24 is agreeable.


| Analytical prediction at neutral surface of 2-D model | Photogrammetric results of I.D. surface | Photogrammetric results of O.D. surface |
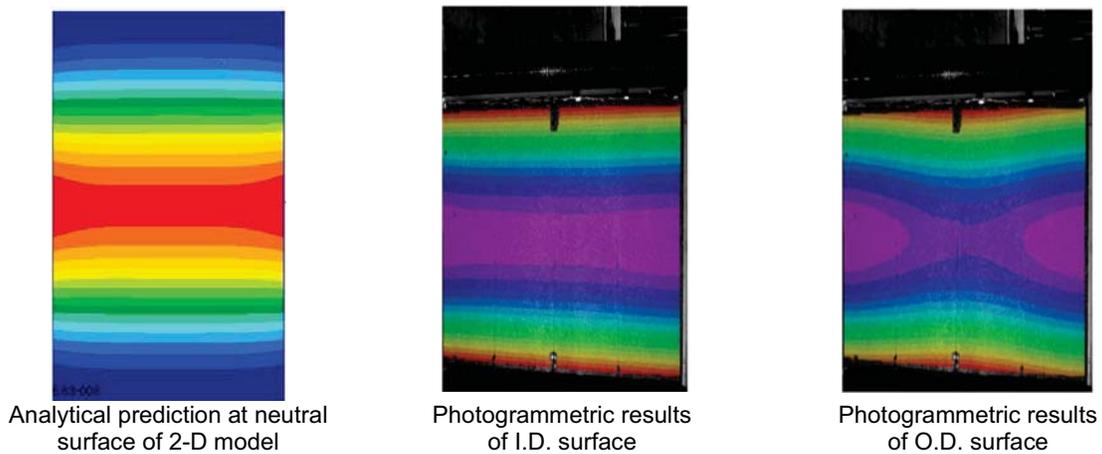
Figure 21.—Post-buckling X (out-of-plane) displacement comparison.

Analytical Predictions   Photogrammetric Results
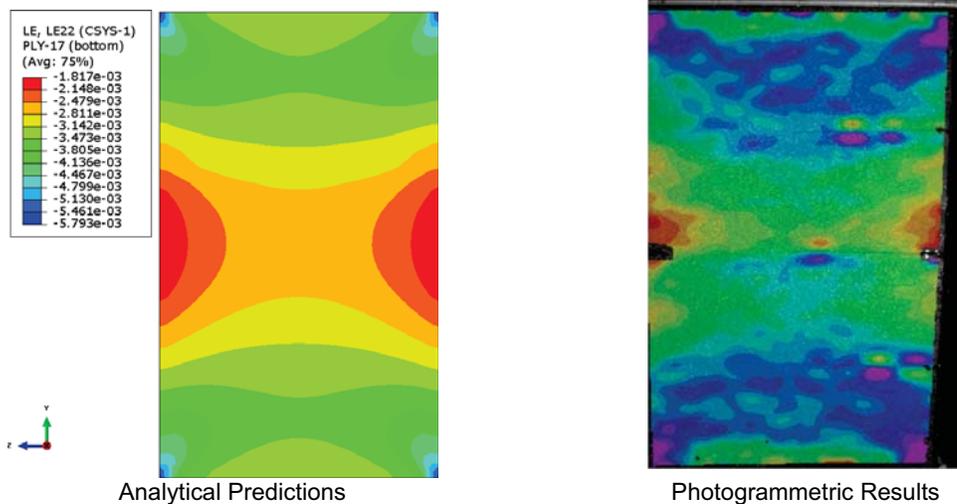
Figure 22.—Post-buckling I.D. minimum principle (Y) strain comparison.
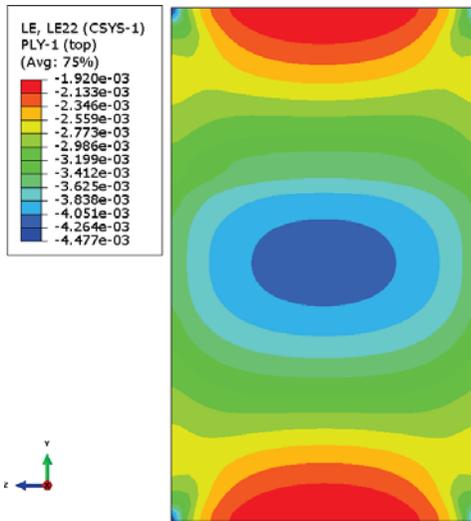
Analytical Prediction

Figure 23.—Post-buckling O.D. minimum principal (Y) strain comparison.
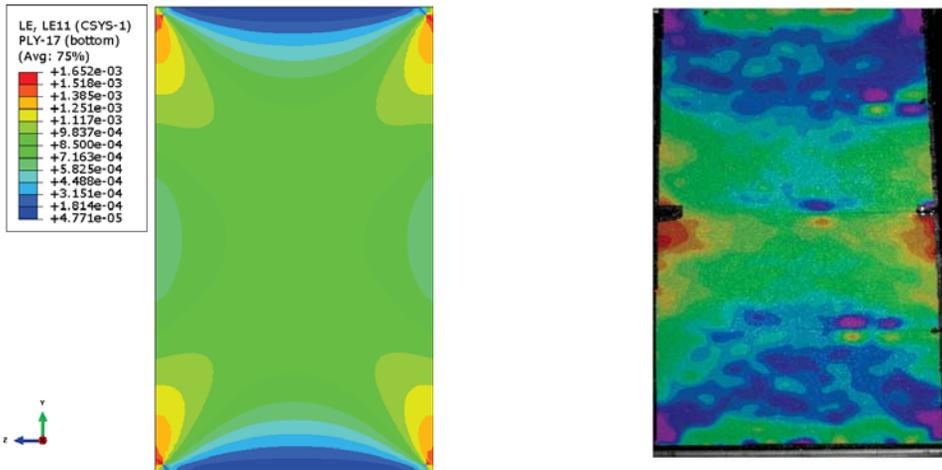
Analytical Predictions   Photogrammetric Results

Figure 24.—Post-buckling I.D. maximum principle (Z) strain comparison.
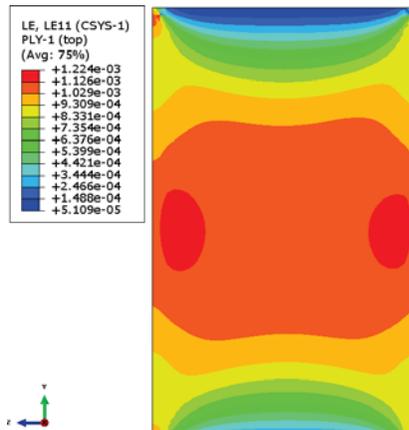

Analytical Prediction

Figure 25.—Post-buckling O.D. maximum principle (Z) strain comparison.
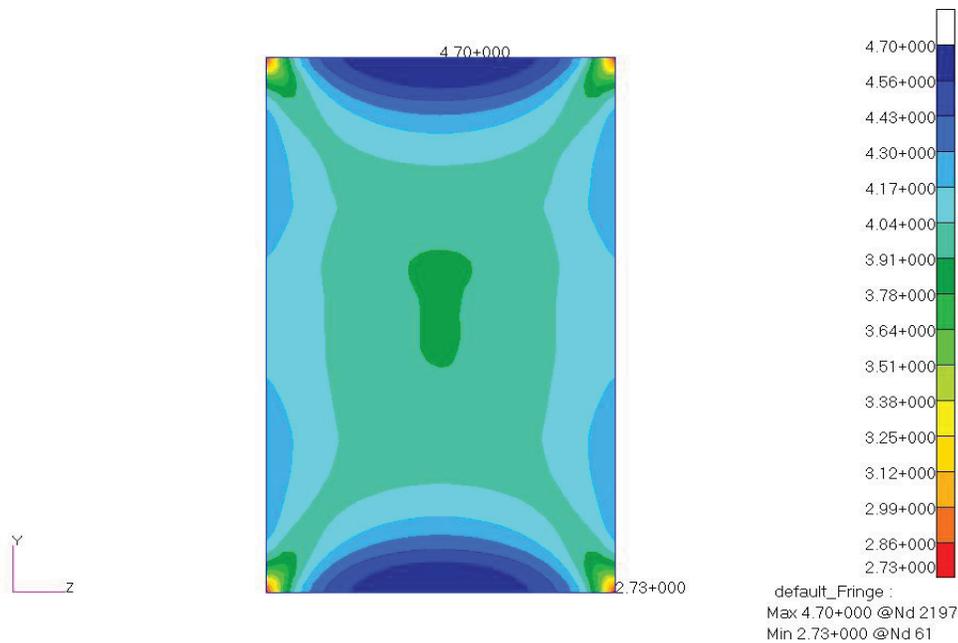
Figure 26.—Strength ratio plot at buckling load.

4.3   Strength Analysis at Buckling Load

In a separate linear static analysis, the panel was loaded up to the buckling load (determined from the non-linear static analysis) using MSC/NASTRAN Sol 101. This analysis was performed to confirm that panel failure was stiffness driven (i.e., the panel would be expected to buckle before it failed in strength). Figure 26 shows the strength ratio plot for the panel at the buckling load. The strength ratio is the local stress versus the allowable, and it incorporates one of three multiaxial failure criteria: Tsai-Wu, Tsai-Hill, Hoffman (Jones, 1999). Figure 26 shows the lowest strength ratio among the three criteria, and all facesheet plies, for each element. The analysis showed that a load 2.73 times greater than the buckling load would be required to fail the panel in strength, indicating the panel is indeed stiffness driven. It should also be noted that the regimes exhibiting the lowest strength ratios are limited to the corners of the panel, while the majority of the panel exhibits strength ratios well above 3.0. The magnitude of the stresses near the corners is likely to be dependent on the size of the elements used in those areas, due to the presence of perfectly sharp corners in the model. Previous studies on different material systems utilizing HyperSizer, a commercially available structural sizing and design software, showed that the strength ratios predicted by HyperSizer and NASTRAN matched well (Myers et al., 2013, Pineda et al, 2013). Furthermore, HyperSizer exhibited positive margins of safety for all other failure modes including core crimping, core crushing, facesheet wrinkling, and facesheet dimpling. Thus, it was deemed unnecessary to repeat this study for this particular material system.

5.0   ANSYS 3-D Finite Element Model

Other studies by Kosareo et al. (2013), Myers et al. (2013), and Pineda et al. (2013) investigated the effects of numerous imperfections on the buckling response of similar sandwich panels containing 8-ply and 6-ply IM7/977-3 facesheets, respectively. The imperfections that were parameterized and studied included the magnitude of the geometric imperfections (bow shape), load eccentricity, fiber misalignment, 3-D effects, and size effects. In this manuscript, only 3-D effects are examined. The reader is referred to Kosareo et al. (2013), Myers et al. (2013), and Pineda et al. (2013) for the other sensitivity studies.

The 3- by 5-ft arc segment sandwich panel was investigated using two different ANSYS finite element models. The first model was a 2-D layered structural shell element from which the results have been presented earlier. The second model was a 3-D layered structural solid-shell element model in which the test fixtures were also included. In ANSYS, the 2-D layered shell element is called a SHELL281 finite element, and the 3-D solid-shell is called a SOLSH190 finite element. These finite element types are shown in Figure 27. A shell element is similar to a NASTRAN quad element, while the solid-shell is similar to a brick element. The SOLSH190 element can be used to model shell structures with a wide range of thickness from thin to moderately thick. Furthermore, the SOLSH190 element formulation permits small thickness to length ratios without producing errors due to large aspect ratios. The thickness between the nodes must equal the sum of the individual layer thicknesses. Otherwise, ANSYS will scale the individual layer thicknesses to fit the actual element thickness. Since the results of the 2-D shell model were included with the ABAQUS and MSC-NASTRAN results in previous sections, these results will only be used as a basis of comparison with the 3-D finite element model.

Figure 28 shows the model of the test panel geometry with the end plates. For clarity, the finite element edges are suppressed. The panel was modeled as 62 in. tall including the 1-in. Al end plates and the 36-in. wide along the chord. The top and bottom 1 in. portions of the panel were supported in the potting material and end plates. Figure 29 shows the slot in the end plate shaped like the arc segment test specimen model. The end of the specimen model is centered in the slot, and the 0.5 in. space around the specimen is filled with solid elements modeling the UNISORB V-100 potting compound with the elastic properties given in Table 6. Each color represents a different material assignment: cyan for the T40-800B/5320-1 facesheets, purple for the honeycomb core, red for the potting compound, and orange for the Al end plates.


SHELL281

2-D 8-Node Structural Shell
with Layered Composite Capability

SOLSH190

3-D 8-Node Structural Solid Shell
with Layered Composite Capability
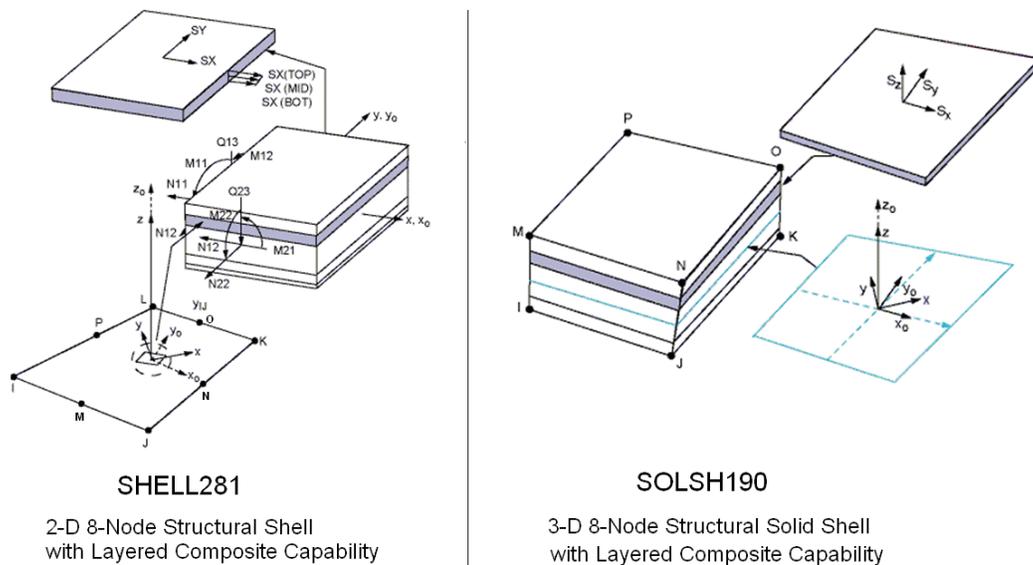
Figure 27.—ANSYS 2-D shell versus 3-D solid-shell (brick) finite elements.

TABLE 6.—ELASTIC PROPERTIES FOR
UNISORB V-100 POTTING COMPOUND

| Property	Value
E, ksi ....436 ksi	
ν 0.35	
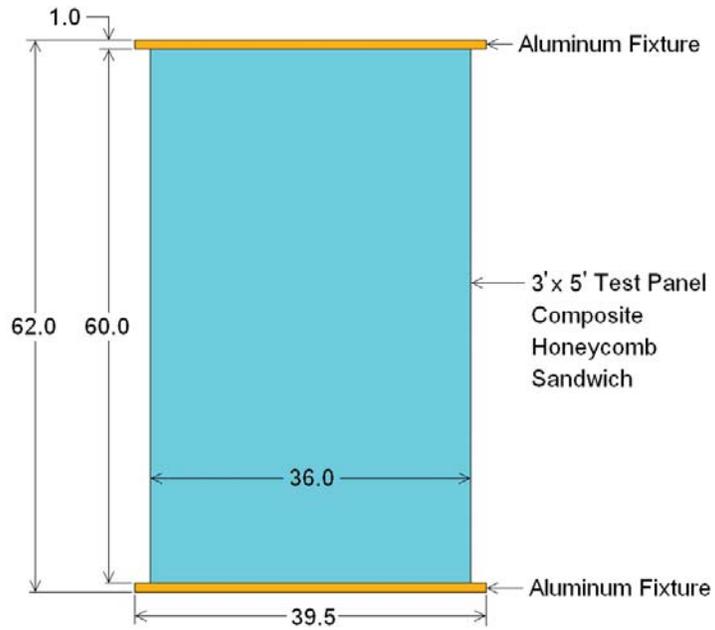
Figure 28.—The 3- by 5-ft arc segment test panel configuration.
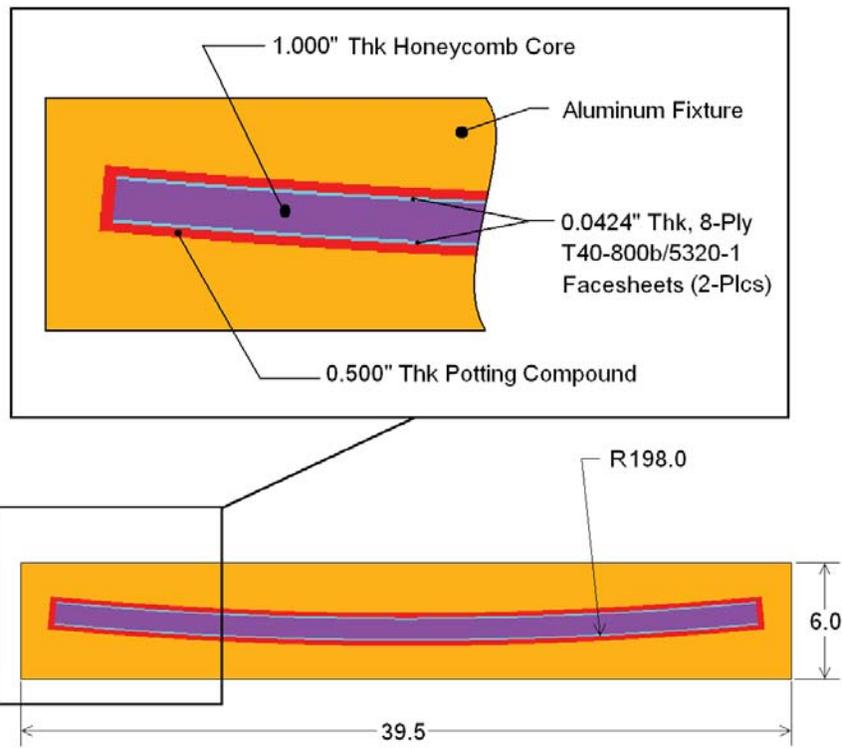
Figure 29.—The 3- by 5-ft arc segment test panel and test fixture end view.
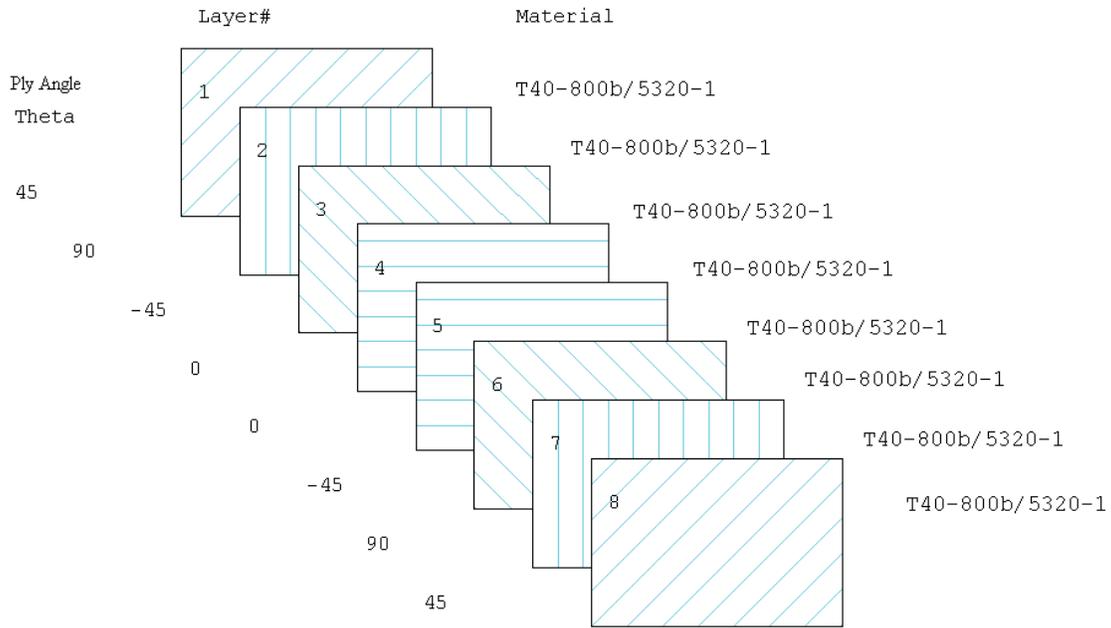
Figure 30 Facesheet 8-Ply T40-800B/5320-1 stacking sequence.

The solid model was generated using a script file containing ANSYS preprocessing, finite element solution, and post-processing commands in the ANSYS Parametric Design Language (APDL) (ANSYS, 2011). The basic geometry, ply stacking sequence, material properties, and geometric imperfections were defined using parameters. The script file can generate the finite element model, perform each analysis in sequence, and process the results in tabular or graphic format.

As shown in Figure 30, the stacking sequence of the facesheets was [45°/90°/–45°/0°]$_s$ with 0.0053 in. thick plies. Again, the T40-800B elastic properties came from test data. Some material data was not available; so IM7/977-3 data was used where T40-800B/5320-1 data was not available. Since IM7/977-3 elastic properties and B-basis allowables were obtained from Orion materials database, they are not listed due to ITAR restrictions (Lockheed Martin, 2010). The Al (5052-T6 alloy) honeycomb properties were obtained from commercially available literature (Hexcell). Unlike the HyperSizer properties, the honeycomb in-plane longitudinal and transverse moduli (E_1 and E_2) were kept at 21.28 psi, and the in-plane shear modulus (G_{12}) was kept at 5.32 psi in the ANSYS models. The honeycomb normal (out-of-plane) modulus (E_3) was also kept at 75 ksi.

The actual panel was secured between two loading platens, with the bottom end plate fixed on the loading platen. The top end plate moved with the top platen in the axial direction. Referring to Figure 31, all three displacements in the solid-shell finite element model were fixed along the bottom edge of the panel and end plate. The same boundary condition was applied to the top panel edge and top end plate, except a displacement was applied in the negative z-axis direction.

TABLE 7.—ANSYS MODEL, Al HONEYCOMB MATERIAL PROPERTIES, 3.1 pcf, 1/8-in.-5052-0.0007 in. THICKNESS

Property/units	Value	Property/units	Value
E_1, psi	21.28	ρ, pcf	3.1
E_2, psi	21.28	F_{t1}, psi	215
E_3, ksi	75	F_{c1}, psi	215
υ_{12}	0.333	F_{t2}, psi	215
υ_{23}	1.0×10^{-5}	F_{c2}, psi	215
υ_{13}	1.0×10^{-5}	F_{t3}, psi	130
G_{12}, psi	5.32	F_{c3}, psi	300
G_{13}, ksi	45	F_{s12}, psi	90
G_{23}, ksi	22	F_{s23}, psi	90
γ, lb/in^3	0.00179	F_{s13}, psi	90
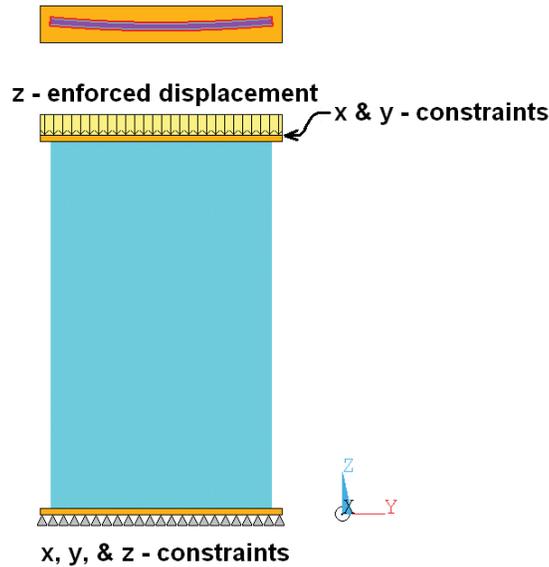
Figure 31.—ANSYS solid model boundary conditions.

It has been shown in this paper that the initial geometric imperfections have an impact on the buckling load and direction. Intuitively, a curved panel is expected to buckle towards the O.D. However, this 3- by 5-ft arc segment test panel buckled toward the I.D., which was primarily due to its bowed shape. Therefore, the initial imperfect geometry is important in a nonlinear buckling analysis (Hong and Jun, 1989). If the 3- by 5-ft panel is modeled as perfectly symmetric (i.e. in geometry and loading), nonlinear progressive collapse does not occur numerically in ANSYS.

One way to introduce anti-symmetry to the model is to apply small perturbations to the applied loads or enforced displacements. This method is not ideal, because it is difficult to determine how to redistribute the loads. Furthermore, varying the load across the top of the panel too drastically could change the problem completely. Another way to introduce anti-symmetry is to superimpose small geometric imperfections (similar to those caused by manufacturing) on the model to trigger the buckling responses. One way to generate these imperfections is with pseudo-random shapes, where the coordinates of the nodes are slightly modified with random amplitudes. The disadvantage in using random imperfections is that they cannot be repeated, and the results would differ for each analysis of the same panel. An easier way to impose geometric imperfections on the finite element model is to employ the linear (Eigen) buckling mode shapes.

The buckling analysis of the 3- by 5-ft arc-segment panel requires several steps. First, the initial bow shape is imposed across the width of the panel model. The imperfections are obtained by running a

preliminary linear buckling analysis, then updating the geometry of the finite element model to the deformed configuration. This technique is done by adding the displacements from the mode shapes multiplied by a scaling factor. The scaling factor is on the order of the manufacturing tolerances and initial bowed shape. A factor of -0.02000 in. was chosen for the 3- by 5-ft panel. Furthermore, the scaling factor was negative to correspond to the direction of the initial bow shape. Applying a positive value could bring the panel model back to a near perfect condition. The imperfections are also added as a sum of the first 10 modes shapes extracted in the preliminary linear buckling analysis as shown in Figure 32. The first 10 mode shapes were used to avoid any bias in the imperfections. Figure 33 shows the resulting geometry.

After the geometric imperfections are added to the finite element model, the nonlinear buckling analysis is performed. In ANSYS, a nonlinear buckling analysis is a static analysis with large deflections active. The magnitude of the applied axial compression is extended beyond the first linear (Eigen) buckling mode. In this analysis the compression was increased gradually using 50 small time increments to predict the critical buckling load.

Figure 34 shows the reaction load versus end compression for the linear and nonlinear shell and solid ANSYS models and the actual test data of the 8010-CMDP panel. The two linear buckling analyses over-predicted the buckling load, and the nonlinear shell FEM analyses over-predicted the buckling load. The nonlinear solid FEM is closest to the test result buckling load. In both nonlinear ANSYS analyses, the panel stiffness was nearly the same.
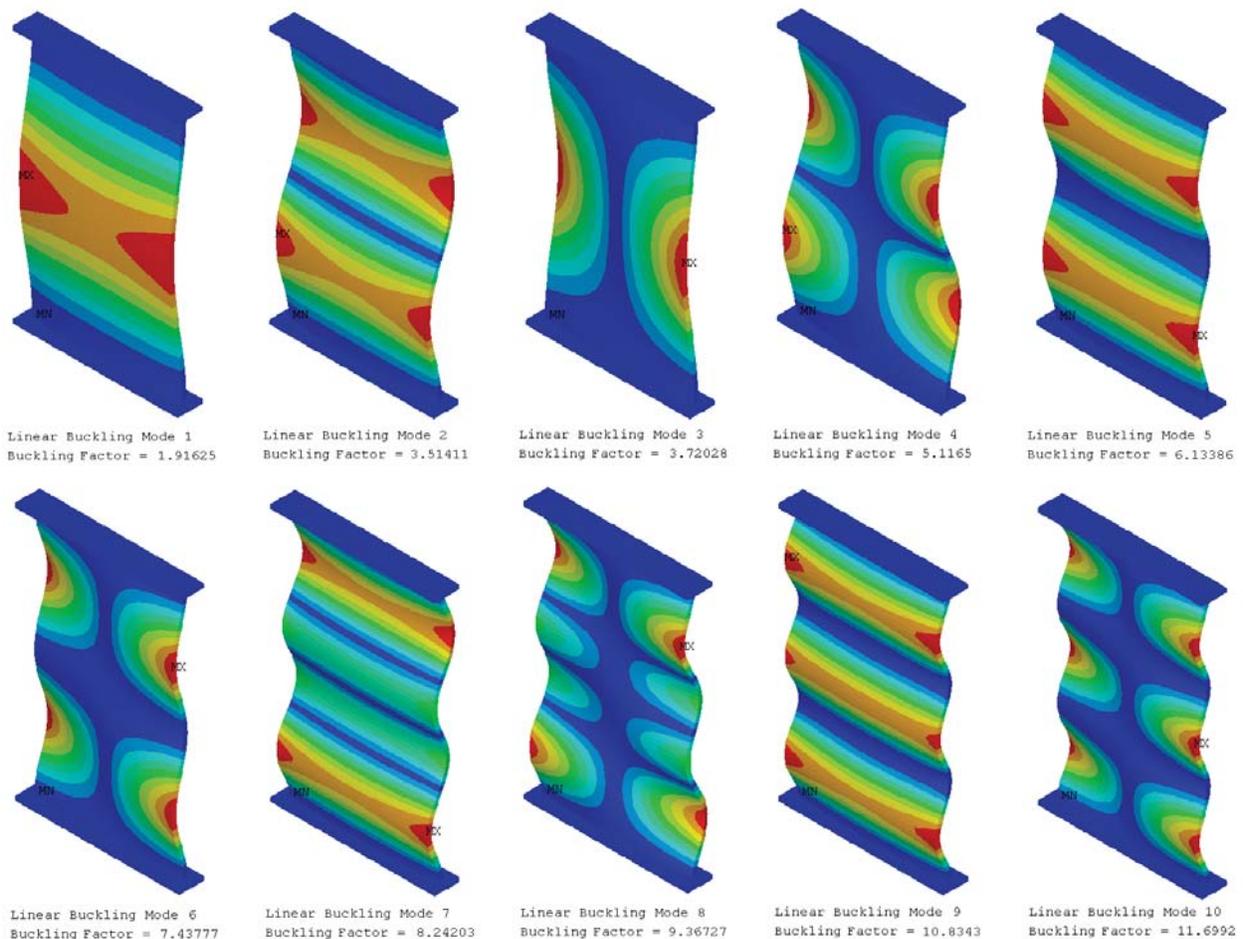

Figure 32.—The first 10 linear buckling mode shapes for the 3x5 panel with 8-ply T40-800B/5320-1 facesheets.
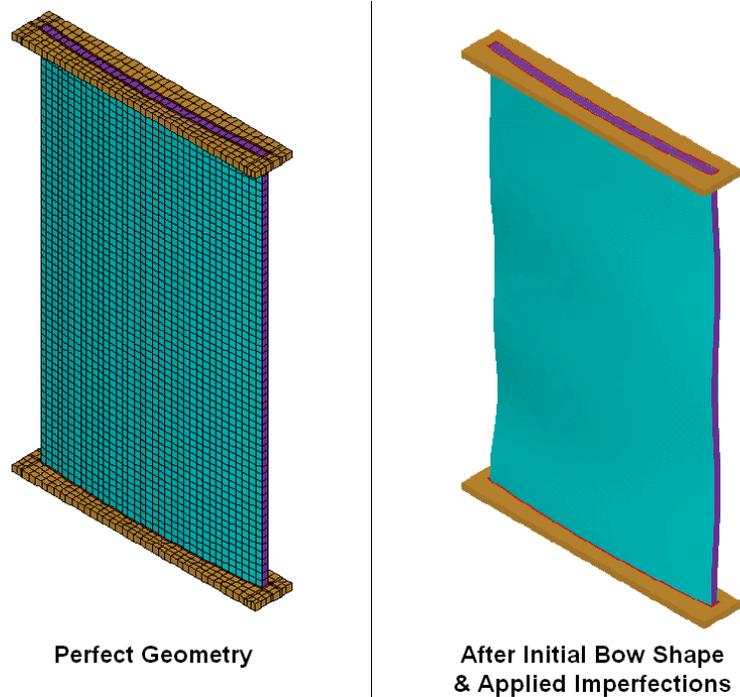
Figure 33.—Panel model with the applied initial bowed shape and geometric imperfections (exaggerated).
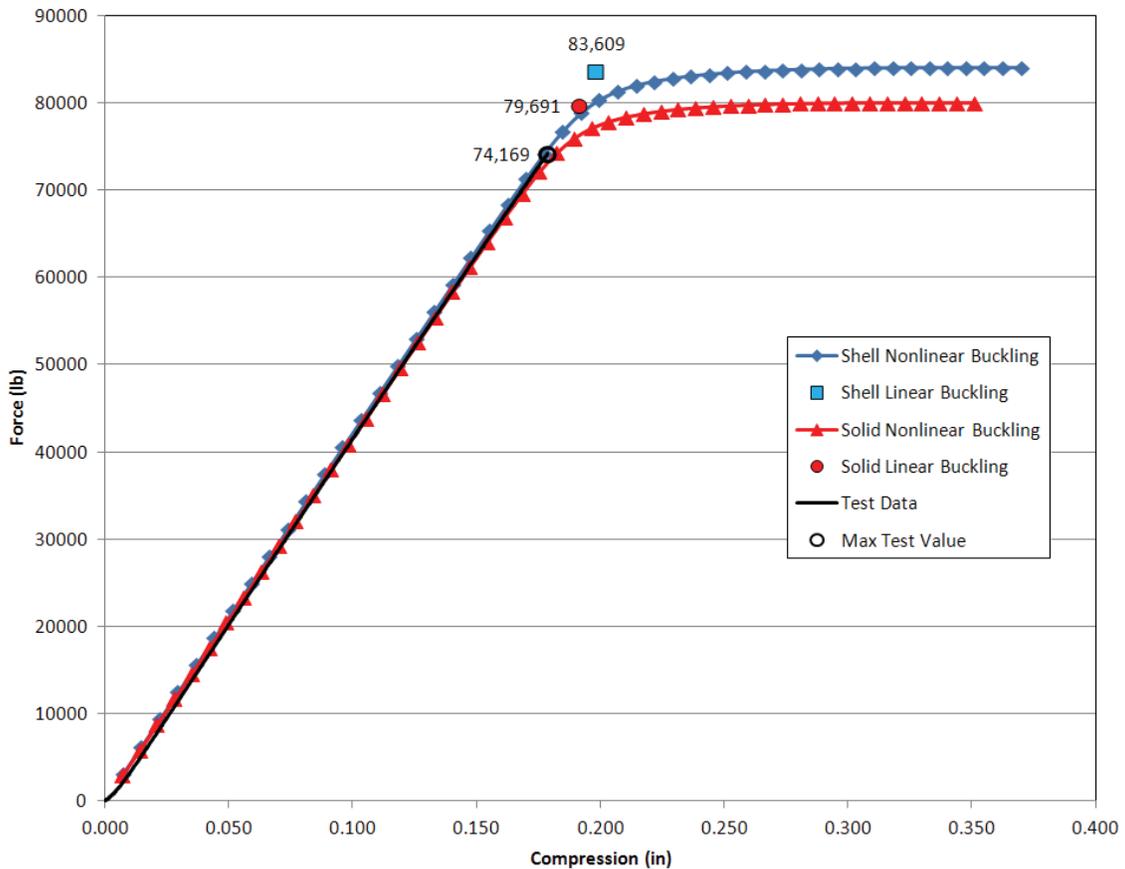

Figure 34.—Total reaction load versus end shortening for ANSYS solid and shell FEM's of 8010-CMDP.
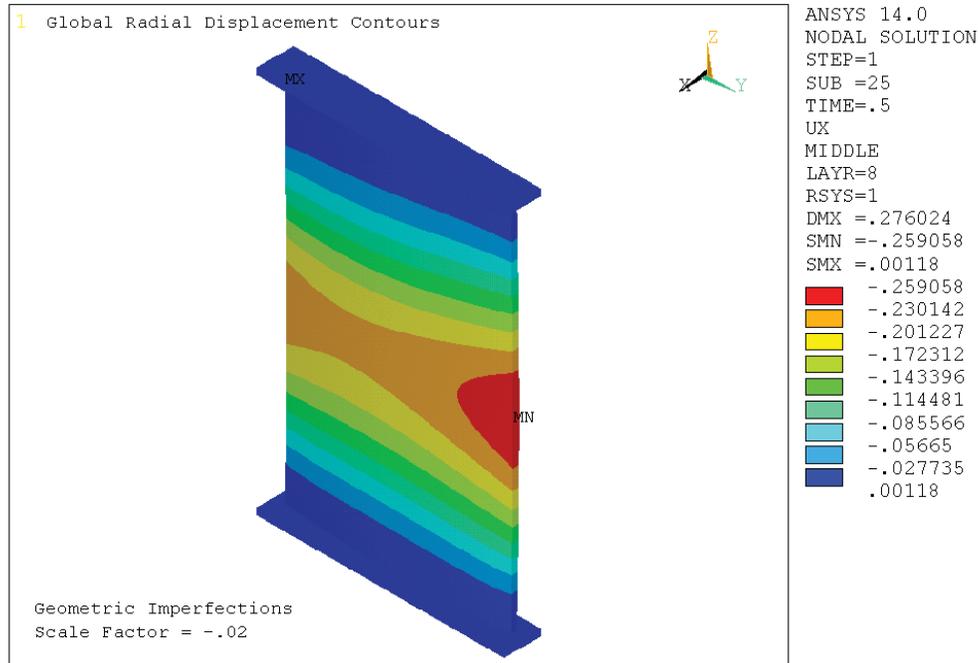
Figure 35.—ANSYS solid FEM, radial displacement contour plot for 8010-CMDP at 0.176-in. end shortening.

Figure 35 shows the panel radial displacement plot (radial component of the total displacement field) when -0.1755 in. was applied to the top edge. As explained earlier, Figure 35 shows the panel buckles in towards the I.D. due to the initial bow and not in the direction of the panel's outer surface. The plot also shows asymmetry in the radial displacements which is also evident in the buckling predictions shown in Table 8. The asymmetry in the radial displacements of Figure 35 is due to the asymmetry in some of the linear buckling mode shapes (as shown in Figure 32) which were superimposed on the original geometry.

Figure 36 shows load versus strain plots for gages located in the center of the panel. On the I.D. side of the panel, the strain goes into compression up to buckling and then starts relieving itself as the load increases during post-buckling. On the O.D. side, the strain remains compressive (negative) suddenly increases in magnitude during post-buckling. The analysis results for the ANSYS shell and solid FEM's show the same trends in strain at that gage location.

Table 8 shows that the first strain reversal occurred at the location of gages 11 and 12, located at the center of the right edge of the panel, at a load of 71,819 lb for the 8010-CMDP panel. Loads corresponding to all strain gage locations are tabulated with the experimental values in Table 8. Note that the buckling load was determined, using the method by Singer et al. (1998), independently from Table 5. Since there is some subjectivity in Singer's method there are some slight discrepancies between the experimental buckling loads in Table 5 and Table 8. Figure 37 and Figure 38 show that, in the corners, the axial O.D. (OML) panel strains went into compression up to the onset of buckling, after which the strain increment reverses and the axial strain is alleviated as the load increases during post-buckling. As pointed out earlier in this paper, this local behavior (observed both experimentally and numerically) is consistent as the panel buckled towards the I.D. Note that, since the major curvature of the panel is biased towards the O.D., the analysis would predict buckling towards the O.D. if no geometric imperfections (or bow) were introduced into the model. Figure 39 shows the strain gage measurements at a panel inflection point at the ¾ panel length location. Figure 40, Figure 41, and Figure 42 show that at the horizontal center of the panel, the I.D. (IML) panel strain goes into compression up to buckling and then starts to reverse as

the load increases during post-buckling. The results from Figure 43 the lower inflection or ¼ length location, match the results from Figure 39. The results in the lower corners from Figure 44 and Figure 45 match the results from the upper corners in Figure 37 and Figure 38, respectively. The error in the nonlinear analyses ranges from 2.56 to 7.13 percent for the 8010-CMDP panel (Table 8), which was an improvement over the linear analyses.
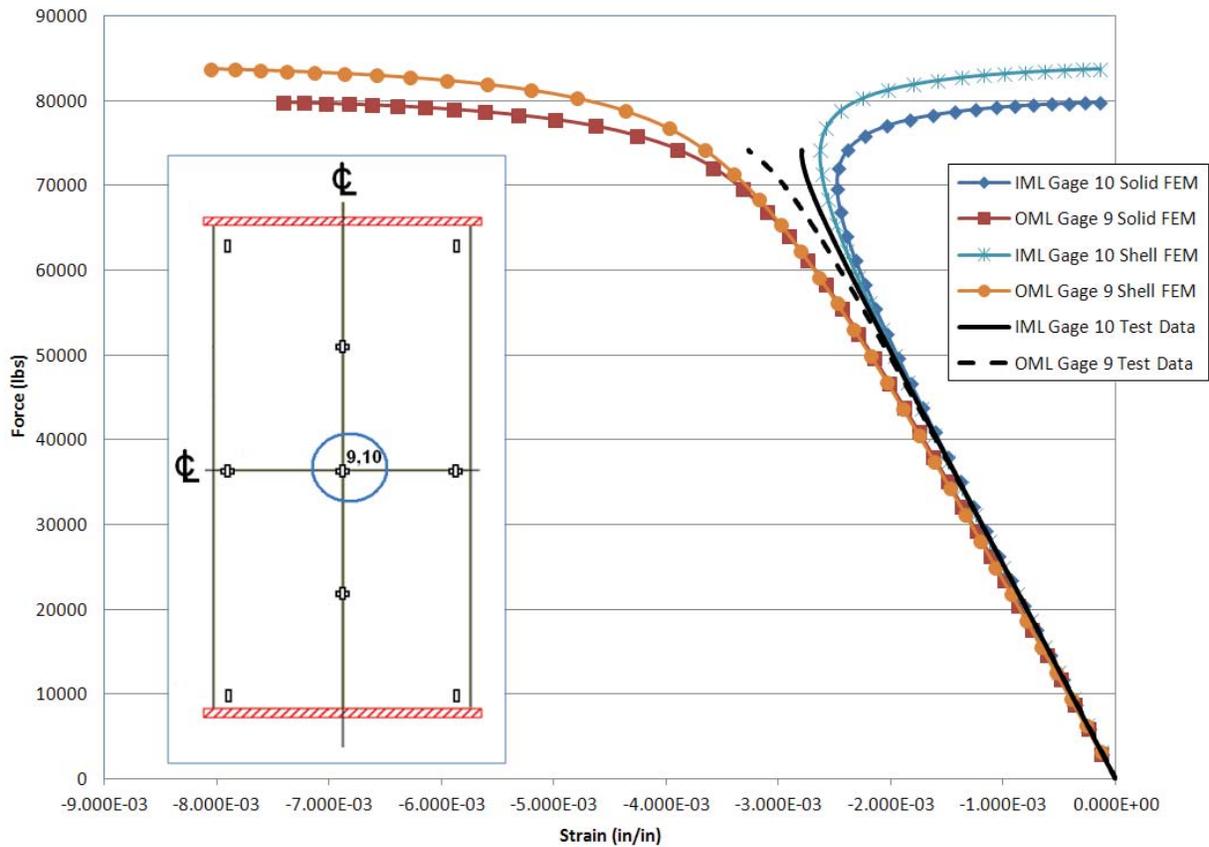

Figure 36.—Load versus minimum principal strain plot for 8010-CMDP at gages 9 and 10.

TABLE 8.—APPROXIMATE TEST AND ANALYSIS
PREDICTION BUCKLING LOADS FOR 8010-CMDP

Gage	Test, lb	Analysis, lb	Error, %
1,2	74,149	72,073	2.80
3,4	74,066	72,073	2.69
7,8	71,964	66,836	7.13
9,10	73,592	69,548	5.50
11,12	71,819	66,836	6.94
15,16	74,169	72,073	2.83
17,18	73,963	72,073	2.56
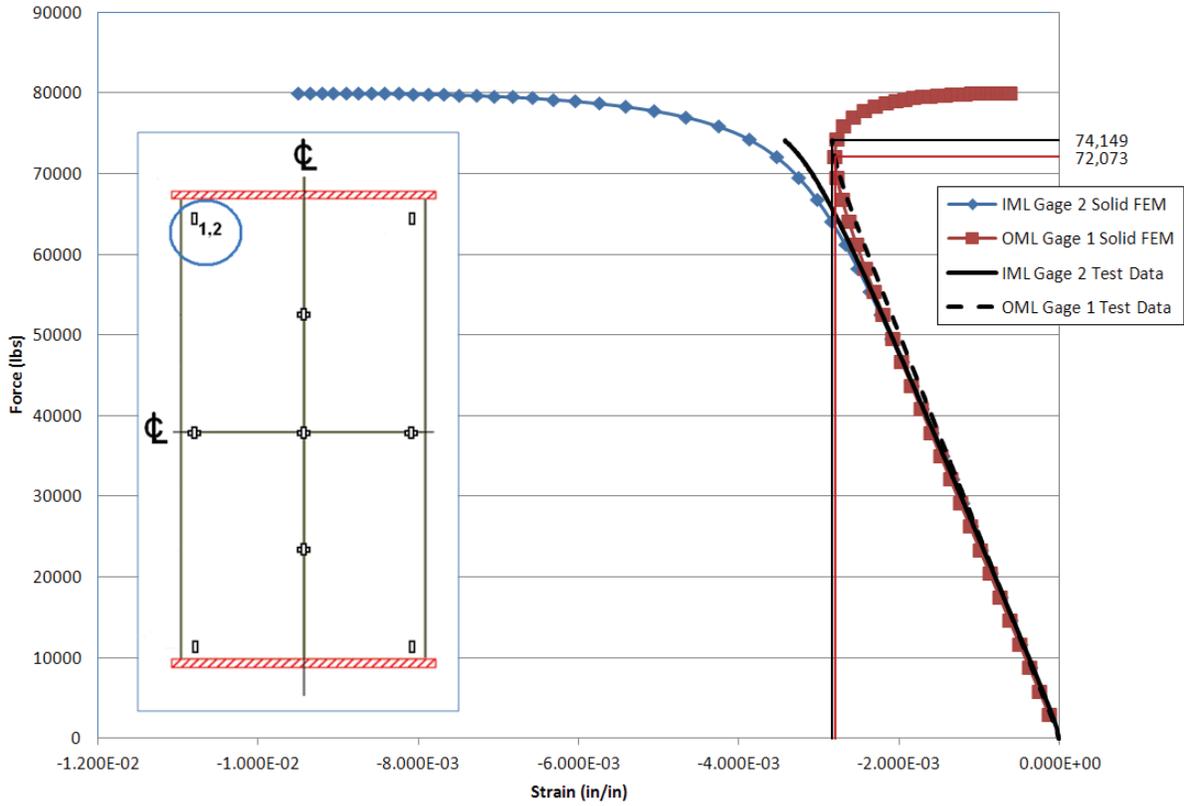
Figure 37.—Load versus minimum principal strain plot for gages 1 and 2.
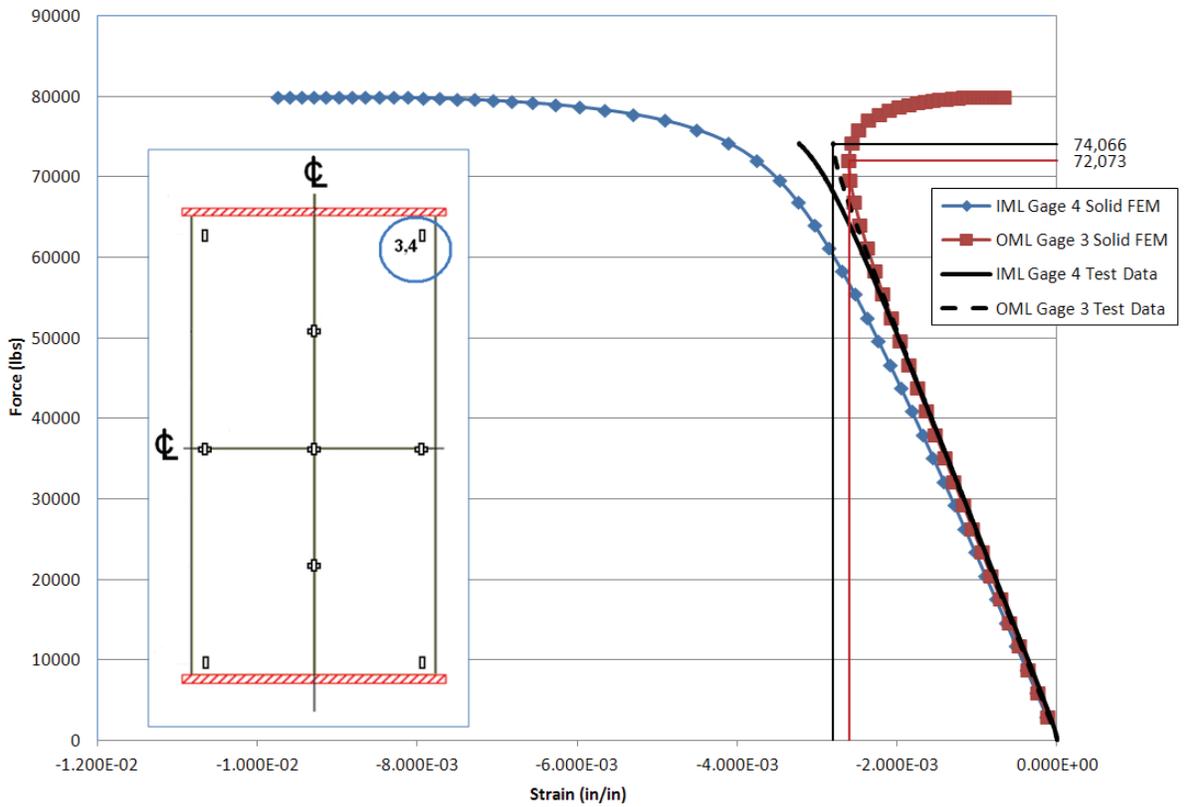
Figure 38.—Load versus minimum principal strain plot for gages 3 and 4.
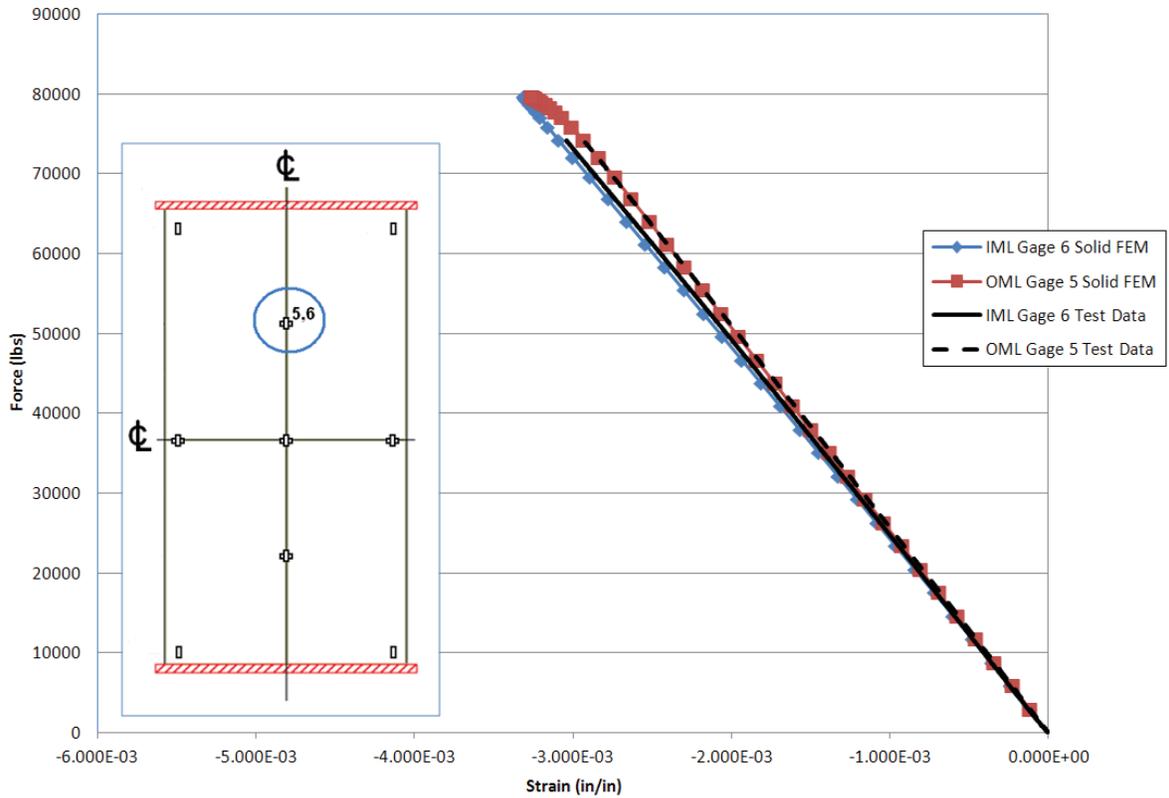
Figure 39.—Load versus minimum principal strain plot for gages 5 and 6.
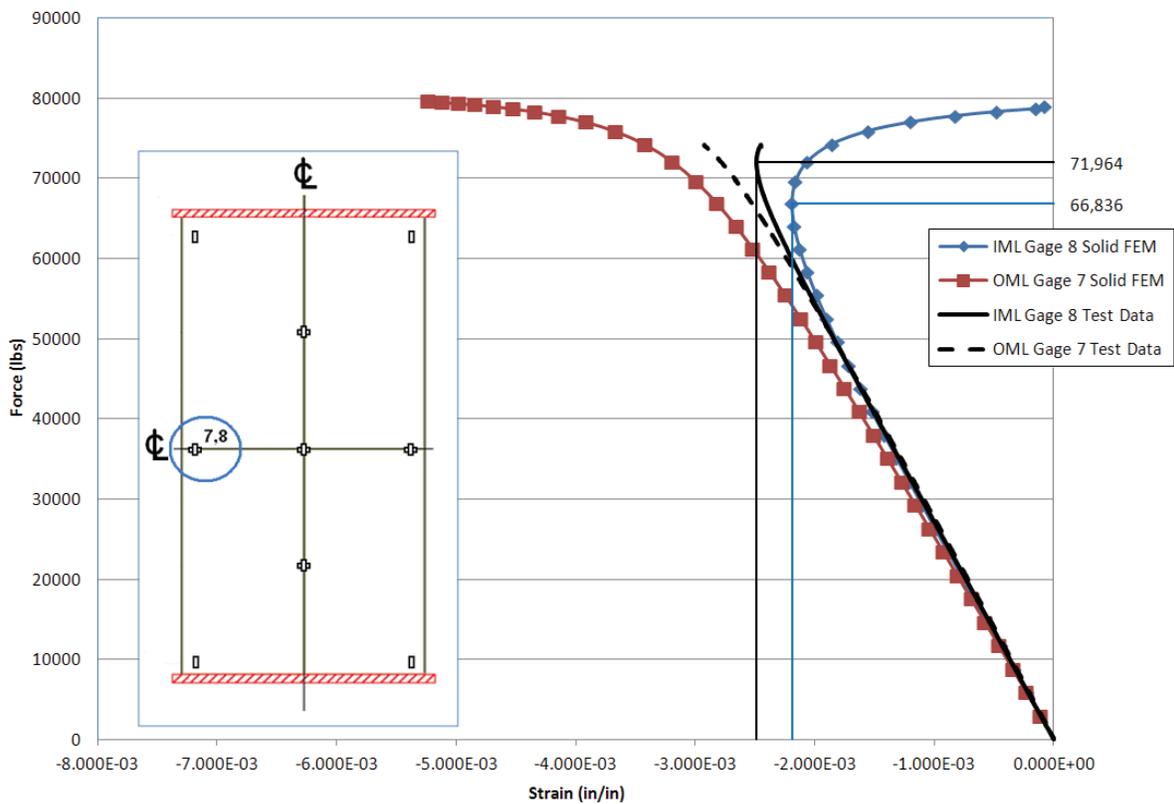
Figure 40.—Load versus minimum principal strain plot for gages 7 and 8.
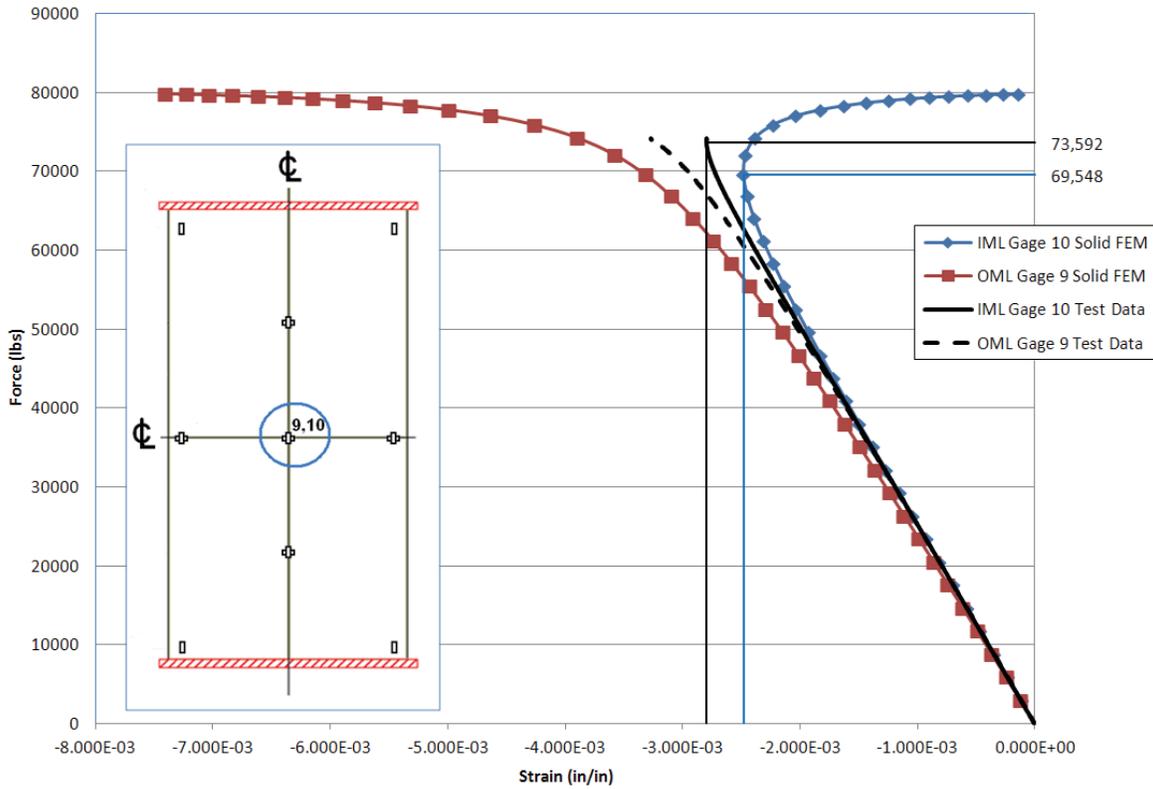
Figure 41.—Load versus minimum principal strain plot for gages 9 and 10.
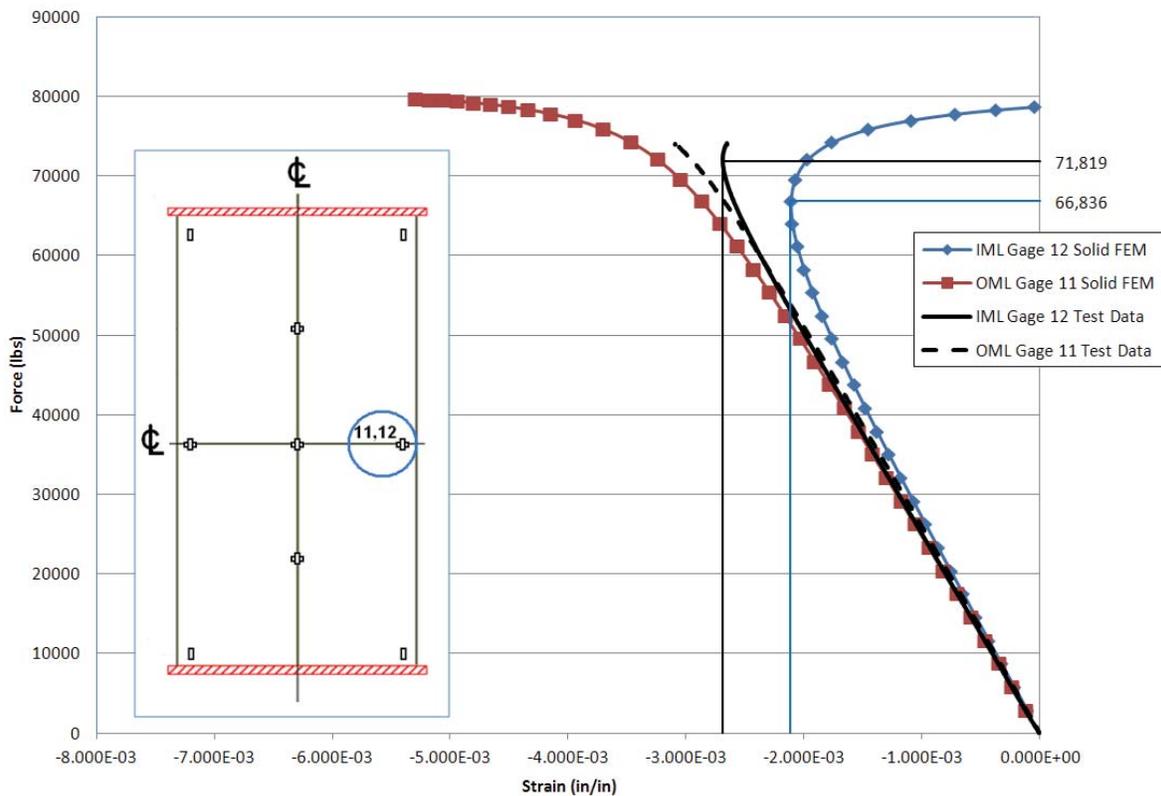

Figure 42.—Load versus minimum principal strain plot for gages 11 and 12.
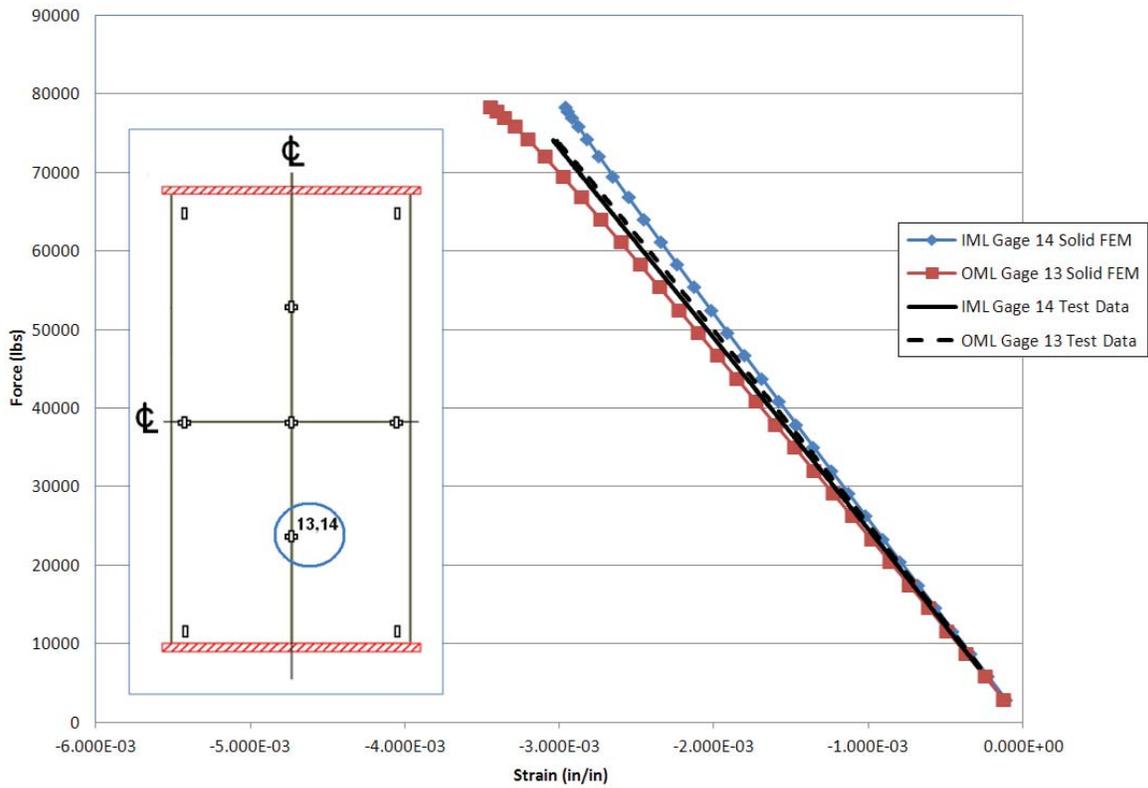
Figure 43.—Load versus minimum principal strain plot for gages 13 and 14.
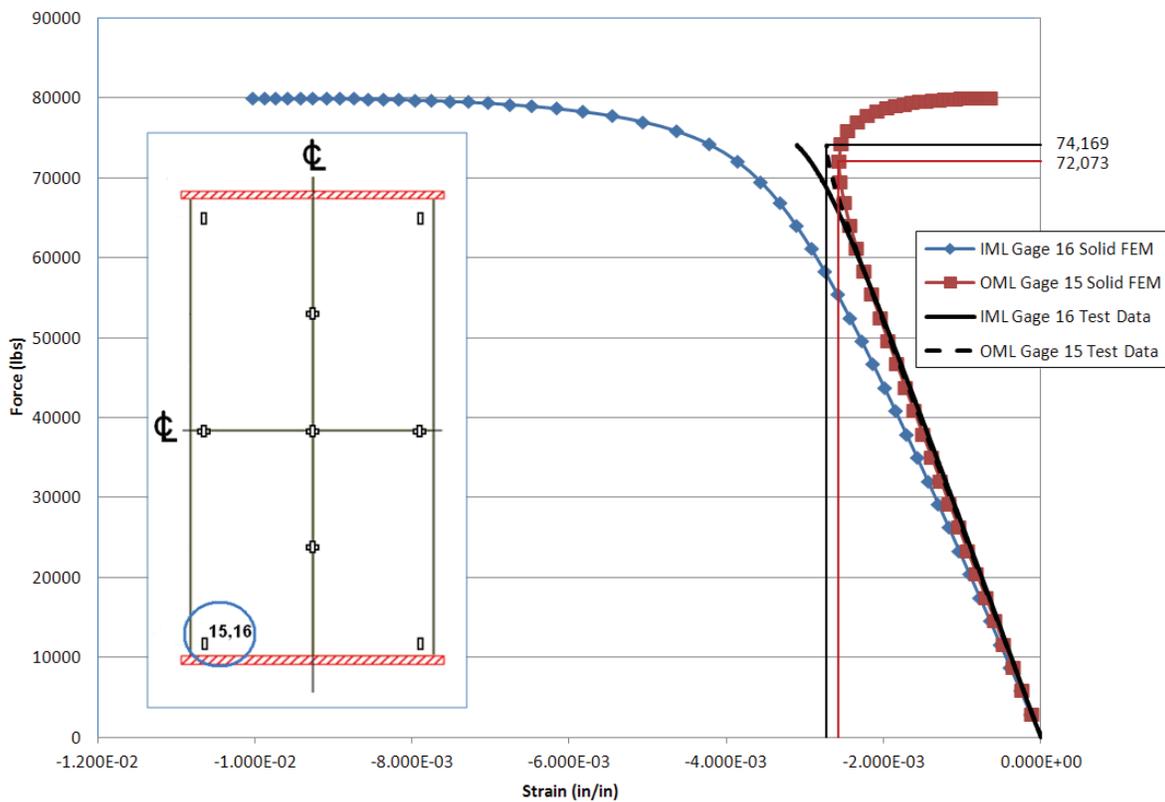
Figure 44.—Load versus minimum principal strain plot for gages 15 and 16.
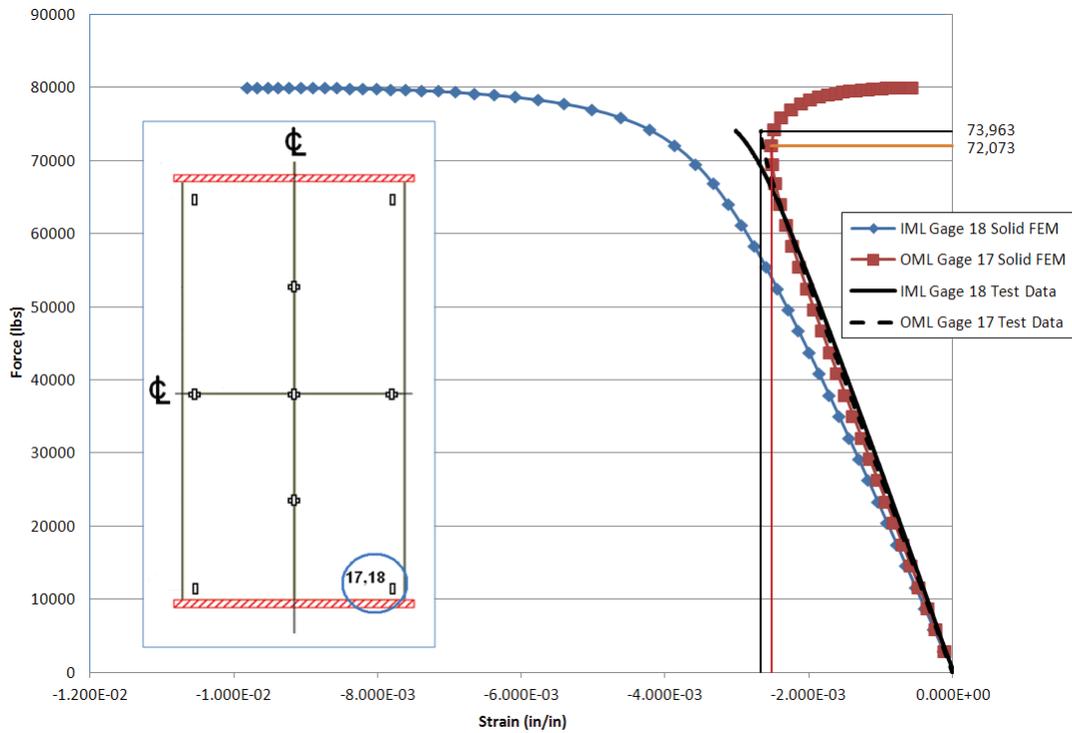
Figure 45.—Load versus minimum principal strain plot for gages 17 and 18.

Figure 46 and Figure 47 show that the post-buckled, in-plane or longitudinal displacement photogrammetry results at 70,062 and 74,168 lb qualitatively compared well with the analytical predictions. In the ANSYS solid element model, the nodal displacements vary slightly on the O.D. and I.D. surfaces. Figure 48 shows the evolution of the in-plane or longitudinal displacement on the I.D. surface, obtained from the numerical analysis, as the applied compressive load is increased. Figure 49 shows the evolution of the in-plane or longitudinal displacement on the O.D. surface, and the contour bands along the top and bottom are thicker. Figure 50 shows that the post-buckled, out-of plane or radial, displacement at 70,062 lb compare well qualitatively with the analytical predictions. Figure 51 shows the evolution of the out-of-plane or radial displacement from the numerical results. The out-of-plane displacements were the same for both the I.D. and O.D. surfaces.

For the I.D. surface, Figure 52 and Figure 53 show that the post-buckled, minimum principal strain test results qualitatively compared well with the analytical predictions at 70,062 and 74,168 lb, respectively. The minimum principal strain (compressive) on the I.D. surface in Figure 54 was fairly uniform up until the point of buckling at 66,836 lb, which is the buckling load predicted at Gages 8 and 12 listed in Table 8 and shown in Figure 40 and Figure 42, respectively. The minimum principal strain was the primary strain in the buckling test. The minimum principal strain (compressive) on the O.D. surface was not uniform through the progression of the applied loads as shown in Figure 55.

The minimum principle strains on the I.D. surface in Figure 54 show the asymmetry in the ANSYS solid FEM, which were a result of the scaled geometric imperfections superimposed from the linear buckling modes. A similar observation is made for the minimum principal strains on the O.D. surface in Figure 55.

Figure 56 and Figure 57 show that the 2nd principal strain also compared well with the in-plane lateral direction. Figure 58 shows the predicted progression of the 2nd principal strain on the I.D. surface from the analysis. The 2nd principal strains in Figure 59 show the asymmetry in the ANSYS solid FEM. Again this was due to the scaled geometric imperfections superimposed from the linear buckling modes.
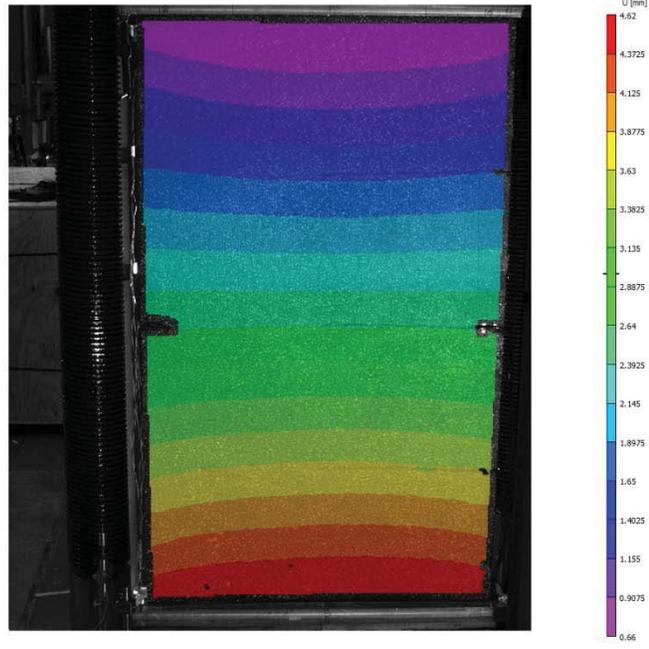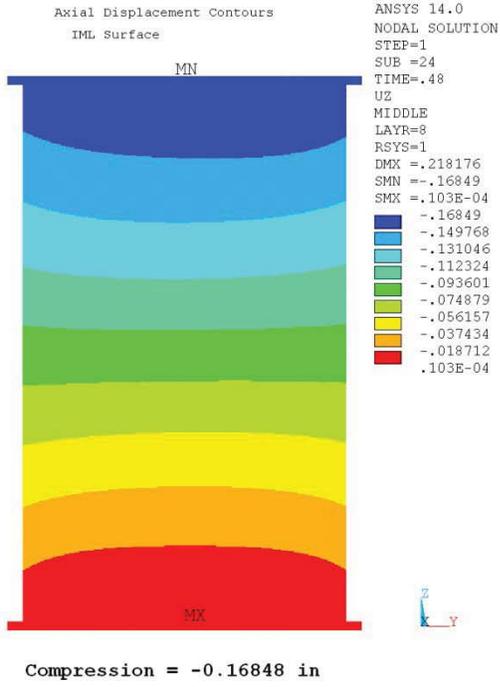
Figure 46.—Post-buckling IML axial (in-plane longitudinal) displacement comparison at 70,062 lb.
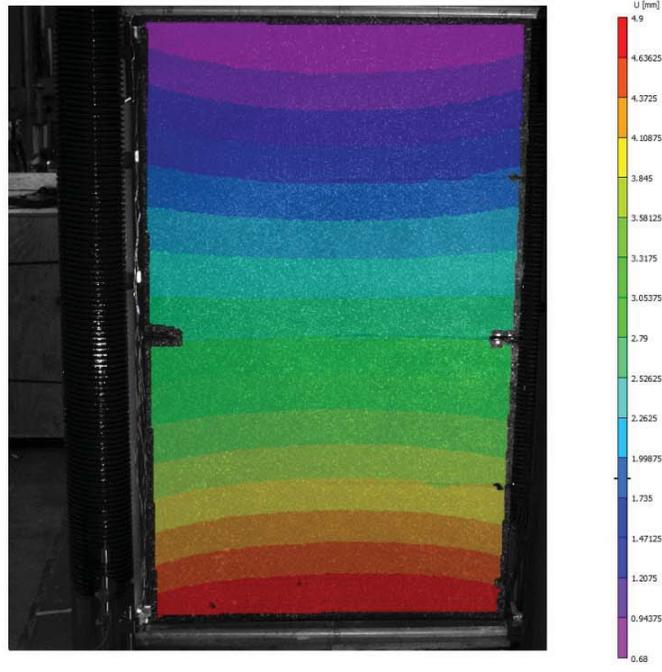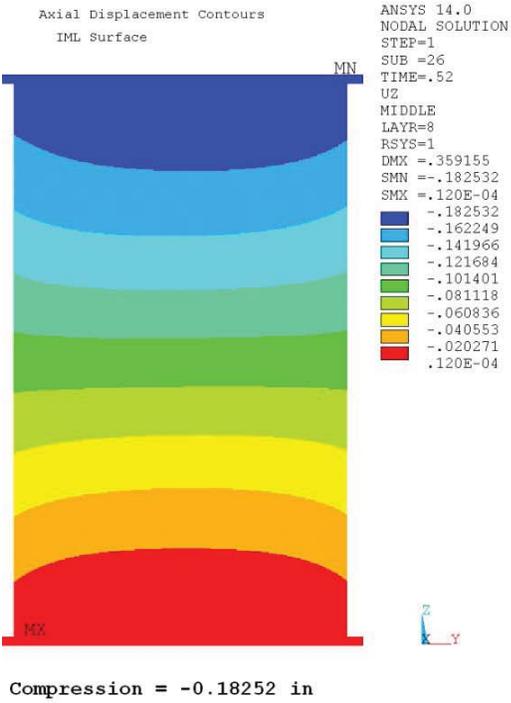

Figure 47.—Post-buckling IML axial (in-plane longitudinal) displacement comparison at 74,168 lb.
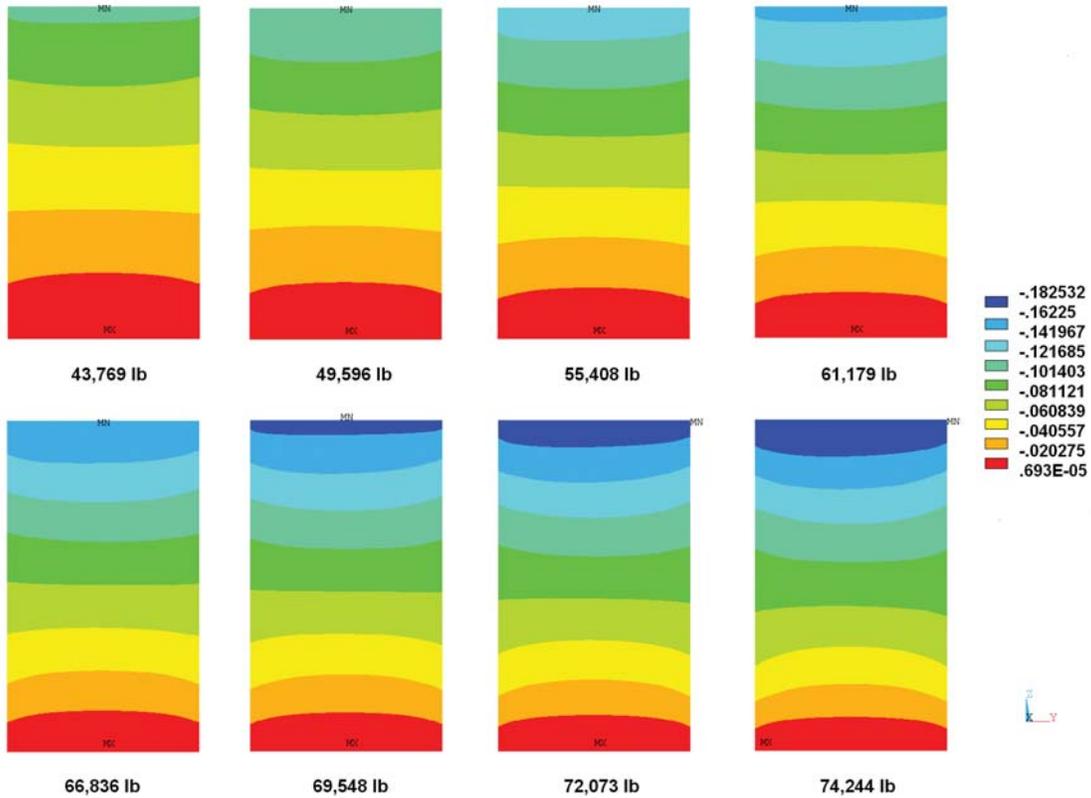
Figure 48.—ANSYS solid FEM, IML axial (longitudinal) displacement contour plots versus load.
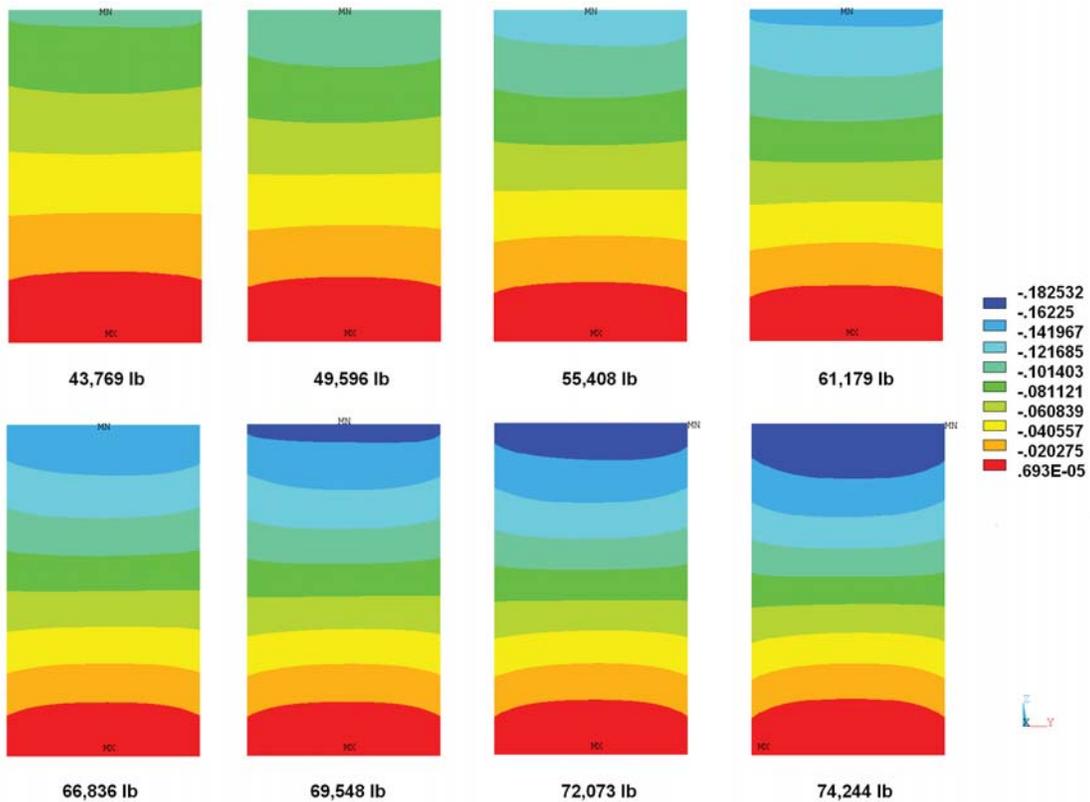

Figure 49.—ANSYS solid FEM, OML axial (longitudinal) displacement contour plots versus load.
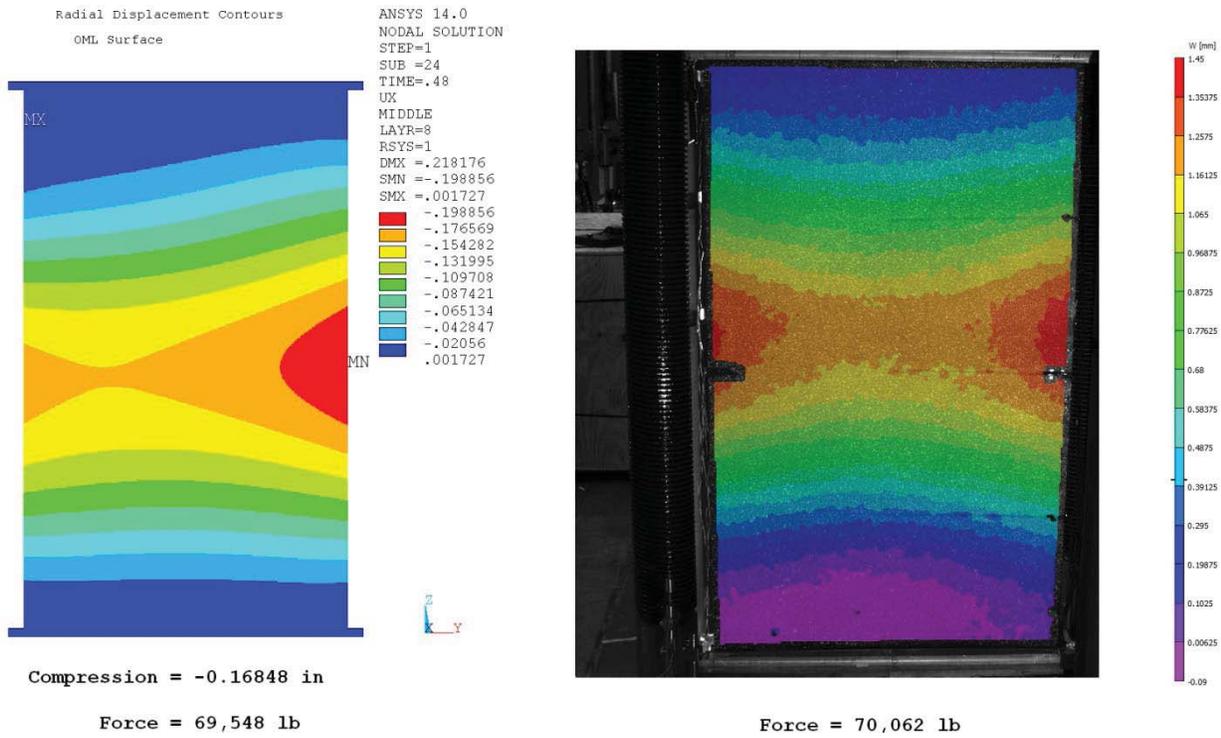
Figure 50.—Post-buckling IML out-of-plane (radial) displacement comparison at 70,062 lb.
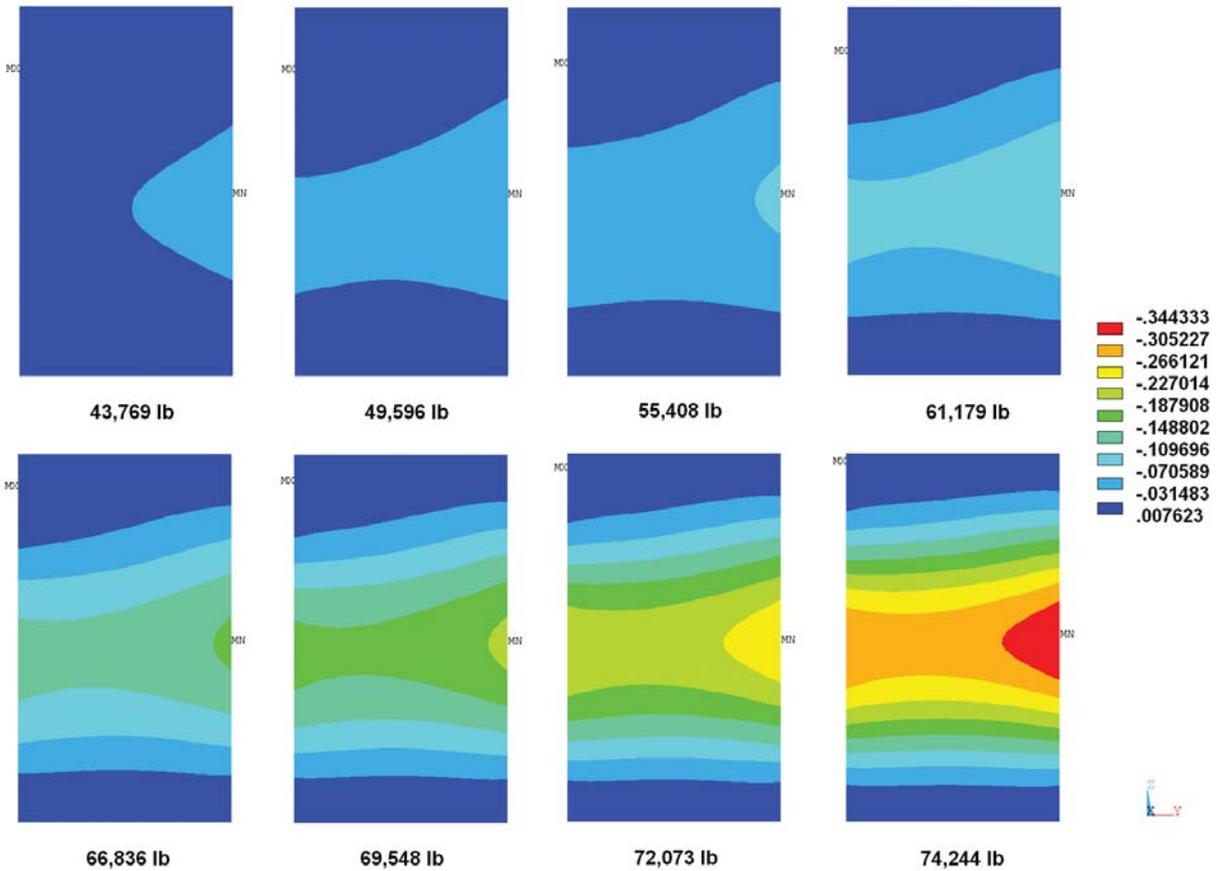

Figure 51.—ANSYS solid FEM, IML and OML out-of-plane (radial) displacement contour plots versus load.
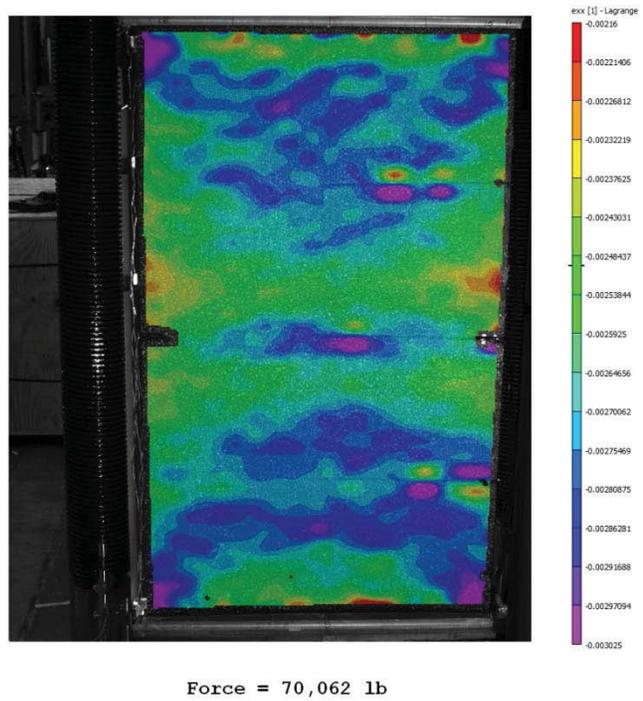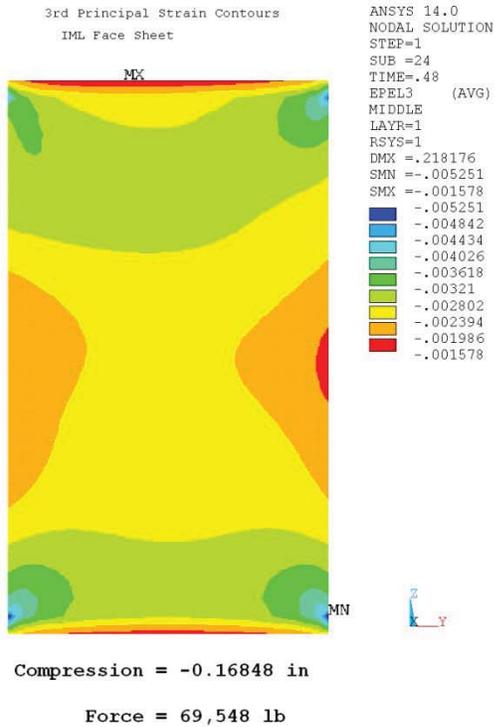
Figure 52.—Post-buckling IML minimum principle (longitudinal) strain comparison at 70,062 lb.
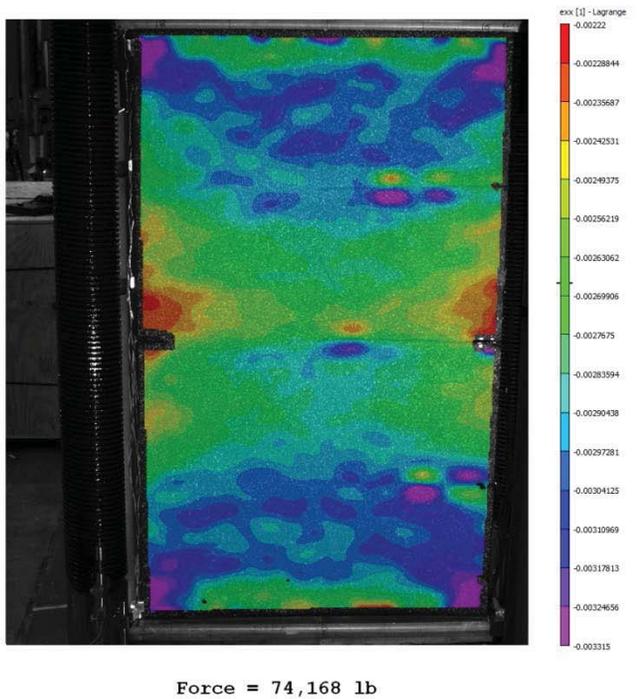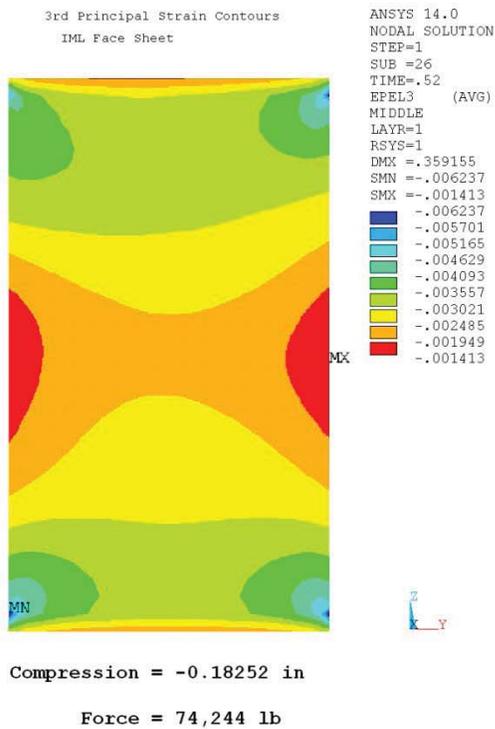

Figure 53.—Post-buckling IML minimum principle (longitudinal) strain comparison at 74,168 lb.
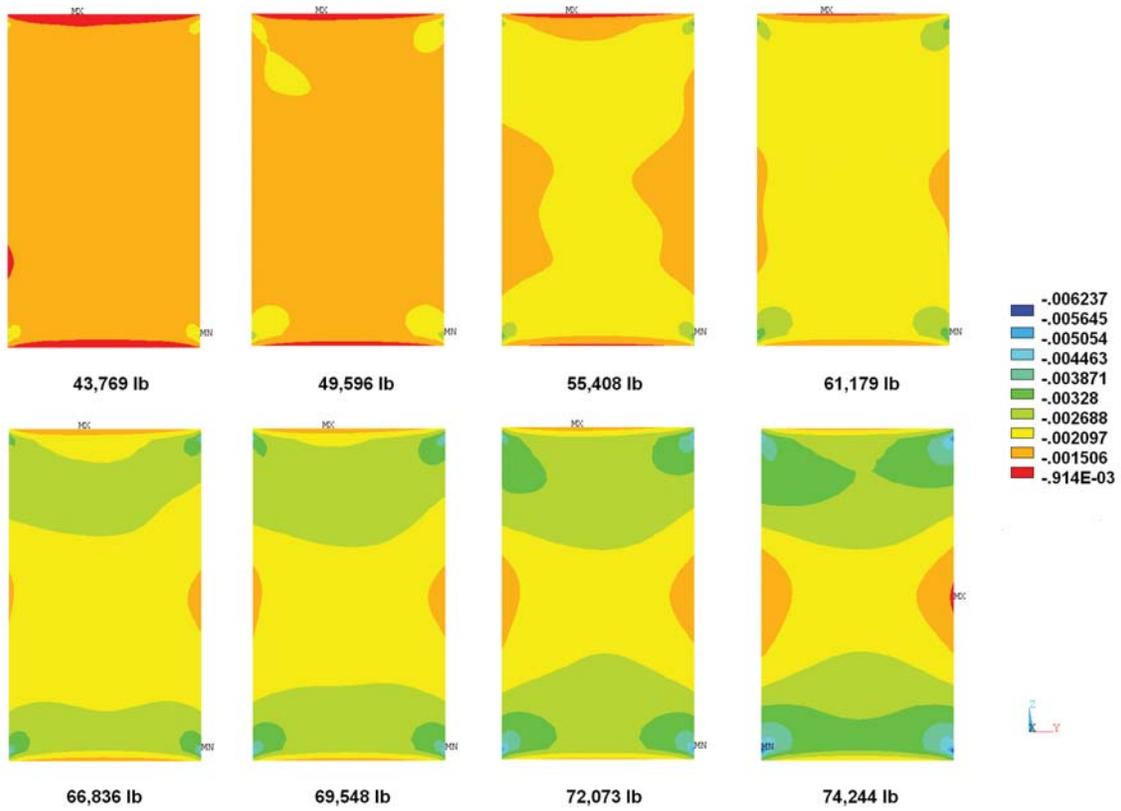
Figure 54.—ANSYS solid FEM, IML minimum principle strain (longitudinal) versus load.
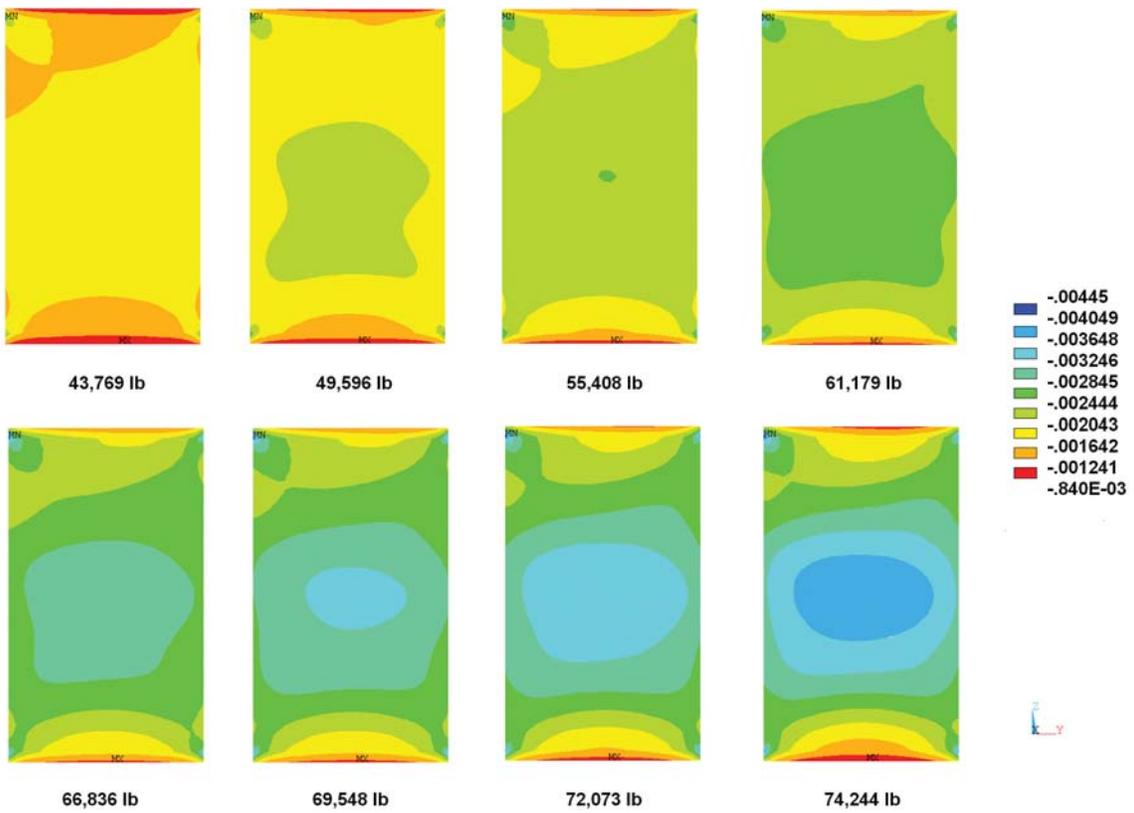
Figure 55.—ANSYS solid FEM, OML minimum principle strain (longitudinal) versus load.
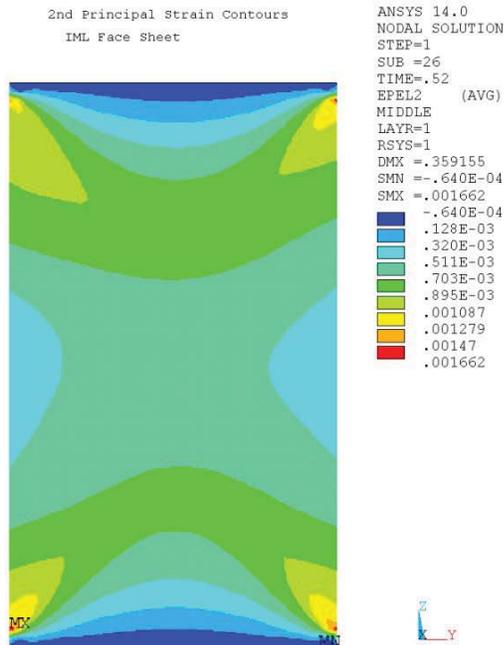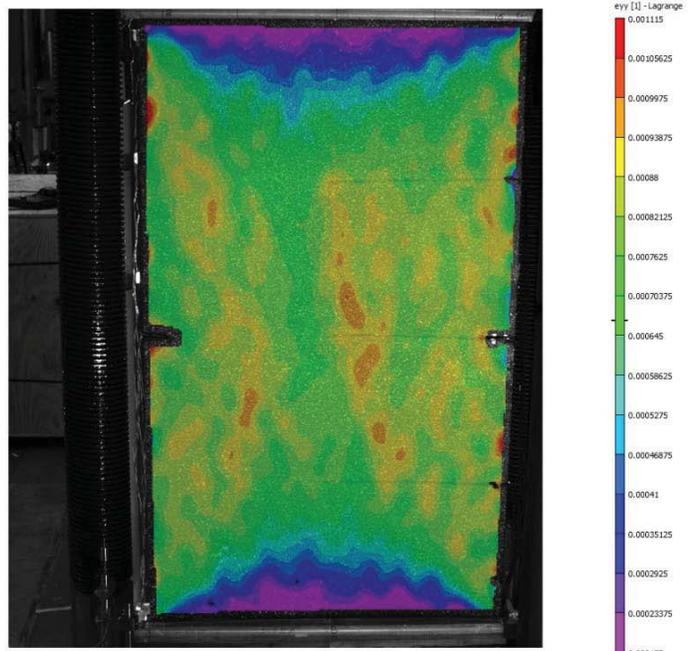
Figure 56.—Post-buckling IML 2nd principle (circumferential or hoop) strain comparison at 70,062 lb.
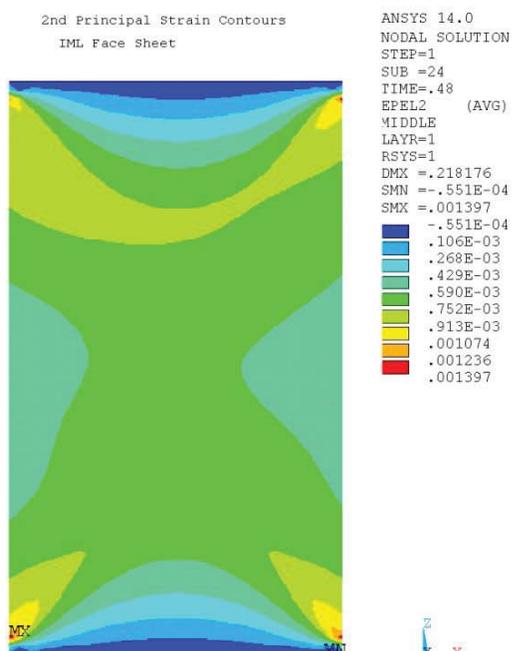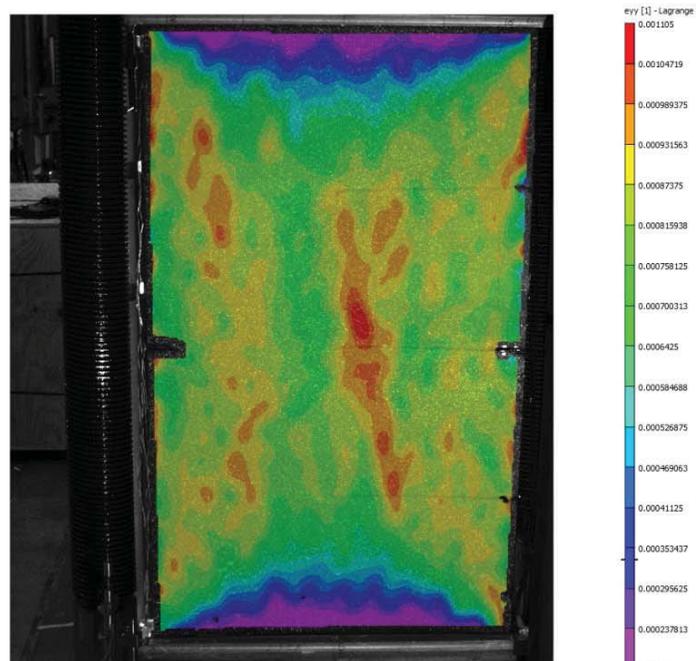
Figure 57.—Post-buckling IML 2nd principle (circumferential or hoop) strain comparison at 74,168 lb.
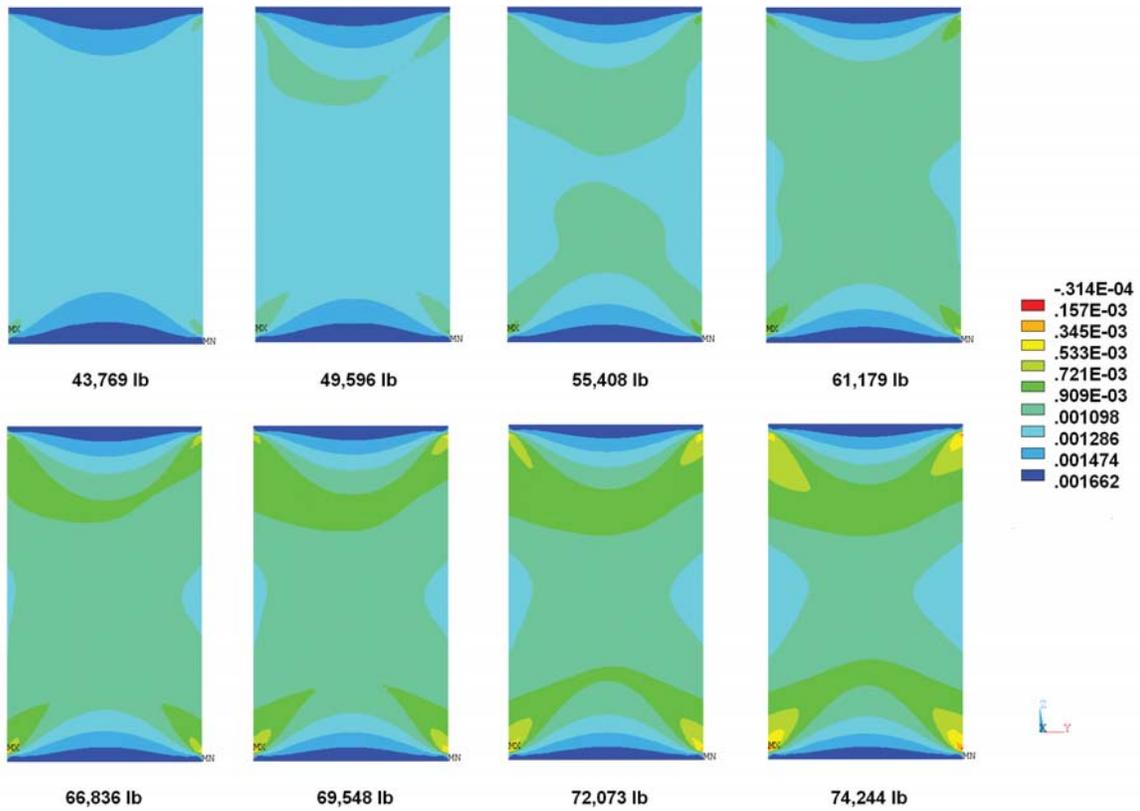
Figure 58.—ANSYS solid FEM, IML 2nd principle (circumferential or hoop) strain versus load.
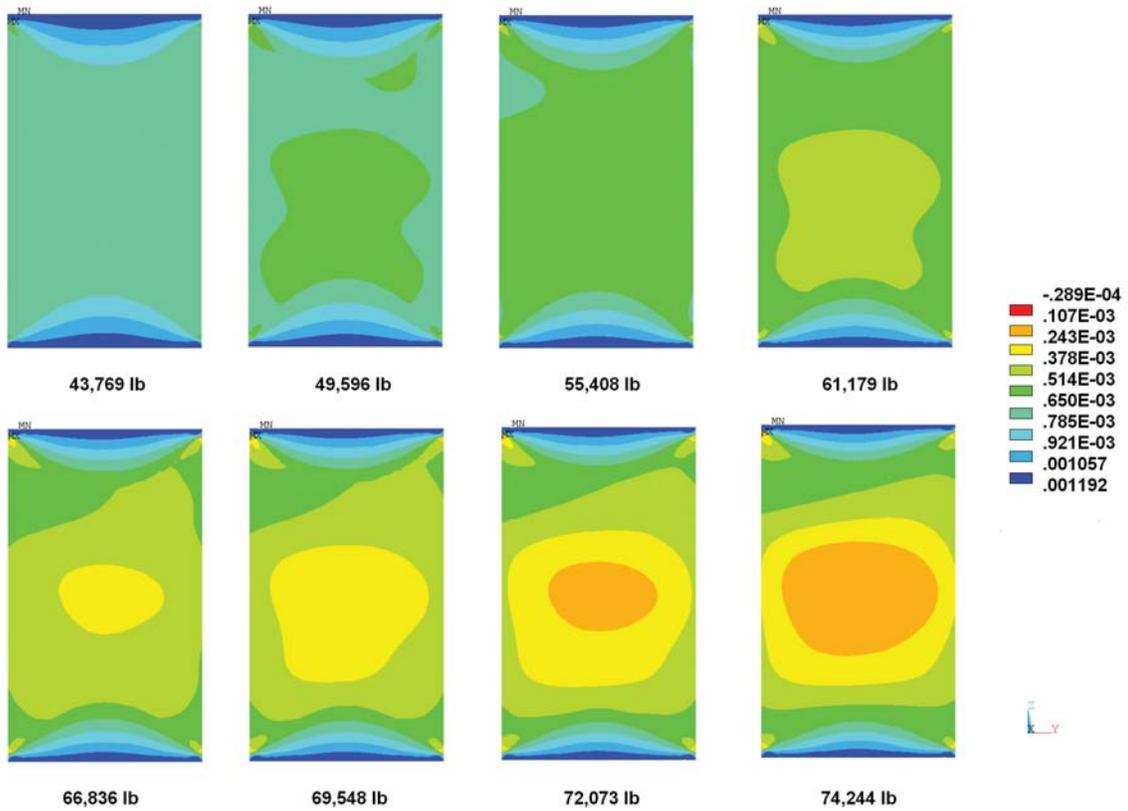

Figure 59.—ANSYS solid FEM, OML 2nd principle (circumferential or hoop) strain versus load.

6.0 Conclusion

Experimental and analytical results have been presented pertaining to the buckling of a 3- by 5-ft, curved, sandwich panel: Panel C (see Table 1). The panel was composed of a 1.000 in. thick Al honeycomb core and 8-ply, quasi-isotropic, OOA cured, T40/800B/5320-1, laminated composite facesheets cut from a 1/16th arc segment of a 10.0 m barrel. Experimental and modeling success was evaluated using specifically defined criteria. Sensitivity studies were not performed for this particular panel, but sensitivity studies were performed to determine the impact of manufacturing defects and documented in previously published manuscripts (Myers et al., 2013; Pineda et al., 2013).

In Section 1.2, the experimental success criteria were described, all of which were met. Namely, all critical instrumentation was fully operational during the test, loads were applied as described in this document, and the maximum attained load and all associated data were recorded and saved. Additionally, the modeling success criteria, described in Section 1.4 were also achieved: the buckling load was predicted within 20 percent, the buckling mode/direction and location was predicted correctly, and the local strain fields correlated well with visual imaging data measured during the experiment.

Both linear eigenvalue and geometrically nonlinear analyses were performed using a variety of commercially available FEM software tools to predict the buckling load of the honeycomb sandwich panel. The linear eigenvalue prediction fell within ~15 percent above the experimental buckling load. Surface imperfection measurements were introduced into the FEM model through a swept bow, and geometrically non-linear analyses were utilized to predict the buckling load via progressive collapse simulations. The simulations yielded a buckling load prediction within ~4 percent (higher) of the experimental load. Furthermore, the direction of buckling (towards the I.D.) and location was predicted correctly, which was a direct consequence of including the measured geometric imperfections in the model. Full field displacement and strain measurements predicted with the nonlinear analysis also corresponded well qualitatively with experimental VIC data. Finally, linear strength analyses were completed at the buckling load, and they ensured that the predicted panel failure was driven by stiffness (i.e., buckling), not strength, as was observed in test.

Shell-based nonlinear buckling analyses of various honeycomb sandwich panel sizes showed that, once again, the buckling predictions of ANSYS, NASTRAN, and Abaqus were in very good agreement. In ANSYS, the first ten linear eigenvalues were used to seed the nonlinear analyses with geometric imperfections. Then, a detailed nonlinear buckling analysis study was performed with an ANSYS solid element model of the 3- by 5-ft arc segment sandwich panel. First, this model was used to show good agreement with the ANSYS shell element based nonlinear model in terms of mode and buckling load. Then, detailed strain histories were examined at various strain gage locations of the test panel. By monitoring the strain histories on the front and back sides of the panel at a given location, it was shown that the point of a strain reversal could be used as an estimate of the onset of buckling. In the solid FEM, analytical predictions of the post-buckled, in-plane or longitudinal displacements compared well with the photogrammetry test results. The analytical predictions of the post-buckled, out-of plane or radial, displacement load compared well qualitatively with the test results. However, contour plots of the analytical out-of-plane or radial displacements do not compare well with the photogrammetry test results. This is primarily due to the seeding of the first ten linear eigenvalues in the nonlinear analyses to produce geometric imperfections. The actual panel imperfections likely drive the shape of the panel's out-of-plane displacements seen in the photogrammetry results. Whereas, the contour shapes from the ANSYS solid FEM are a function of the first ten eigenvalues superimposed on the initial panel geometry.

It can be concluded that, a good buckling load prediction was achieved utilizing shell-based linear eigenvalue analysis in conjunction with nominal (perfect) panel geometry. This prediction was improved by utilizing a more sophisticated, geometrically nonlinear, progressive collapse analysis that incorporated

measured geometric imperfections from the panel. Although the results of these studies cannot be directly applied to obtain better estimates of the buckling loads (beyond eigenvalue analysis) of full cylinders or larger cylinder segments (as the buckling modes and imperfection sensitivities are different for these different geometries), the practices presented here can be used to determine the same sensitivities of these other structures to similar imperfections. In the future, such studies may lead to more comprehensive linear bucking knockdown factors for cylindrical shells that consider the impact and degree of different imperfections or defects separately (Haynie et al., 2012; Hilburger, 2012; Kriegesmann et al., 2012). Furthermore, these sensitivity studies can be utilized to arrive at critical manufacturing tolerances.

References

ANSYS Mechanical Application User's Guide, Release 14.0, 2011 SAS IP, Inc.

Hause, T., Johnson, T. E., Librescu, L., Effect of face-sheet anisotropy on buckling and postbuckling of sandwich plates, Journal of Spacecraft and Rockets, 37(3), pp. 331-341, 2000.

Hause, T., Librescu, L., Johnson, T. F., Non-linear response of geometrically imperfect sandwich curved panels under thermomechanical loading, International Journal of Non-Linear Mechanics, 33(6), pp. 1039-1059, 1998.

Haynie, W. T., Hilburger, M. W., Bogge, M., Maspoli, M. Benedikt, K., Validation of lower-bound estimates for compression-loaded cylindrical shells, 53rd AIAA/ASME/ASCE/AHS/ASC Structures, Structural Dynamics, and Materials Conference, 23-26 Apr., Honolulu, HI, 2012.

Hilburger, M. W., Developing the next generation shell buckling design factors and technologies, 53rd AIAA/ASME/ASCE/AHS/ASC Structures, Structural Dynamics, and Materials Conference, 23-26 Apr., Honolulu, HI, 2012.

Hilburger, M. W., Nemeth, M. P., Starnes, J. H., Jr., Nonlinear and buckling behavior of curved panels subjected to combined loads, 42nd AIAA/ASME/ASCE/AHS Structures, Structural Dynamics and Materials Conference and Exhibit, 16-19 Apr., Seattle, WA, 2001.

Hilburger, M. W., Starnes, J. H., Jr., Effects of imperfections on the buckling response of compression-loaded composite shells, International Journal of Non-Linear Mechanics, 37, pp. 623-643, 2002.

Hong, C. S., Jun S. M., Buckling behavior of laminated composite cylindrical panel with initial imperfections, Winter Annual Meeting of the American Society of Mechanical Engineers, co-sponsored by Pressure Vessels and Piping Division & Aerospace Division, ASME, San Francisco, CA, Dec. 10-15, 1989, PVP-Vol. 183, AD-Vol. 18.

HyperSizer Structural Sizing Software, Collier Research Corp., Newport News, VA, www.HyperSizer.com, 2012.

Jones, R. M., Mechanics of Composite Materials, 2nd Edition, Taylor & Francis, Inc., Philadelphia, PA, 1999.

Kellas, S., Lerch, B., Wilmoth, N., Mechanical characterization of in- and out-of-autoclave cured composite panels for large launch vehicles, SAMPE 2012, Baltimore, Maryland, May 21-24, 2012.

Kosareo, D. N., Oliver, S. T., Bednarcyk, B. A., and Pineda, E. J., "Buckling Design and Analysis of a Payload Fairing 1/6th Arc-Segment Panel," 55th AIAA/ASME/ASCE/AHS/ASC Structures, Structural Dynamics, and Materials Conference, National Harbor, MD, January 2014.

Kriegesmann, B., Hilburger, M. W., Rolfes, R., The effects of geometric and loading imperfections on the response and lower-bound buckling load of a compression-loaded cylindrical shell, 53rd AIAA/ASME/ASCE/AHS/ASC Structures, Structural Dynamics, and Materials Conference, 23-26 Apr., Honolulu, HI, 2012.

Lockheed Martin, Orion Materials and Design Allowables, Rev. D, 22 Sept, 2010.

Ley, R. P., Lin, W., Mbanefo, U., Facesheet wrinkling in sandwich structures, NASA/CR—1999-208994, 1999.

Lynch, C., Murphy, A., Price, M., Gibson, A., The computational post buckling analysis of fuselage stiffened panels loaded in compression, Thin-Walled Structures, 42, pp. 1445-1464, 2004.

Myers, D. E., Pineda, E. J., Zalewski, B. F., Kosareo, D. N., Kellas, S., Buckling testing and analysis of honeycomb sandwich panel arc segments of a full-scale faring barrel – Part 1: 8-ply in-autoclave facesheets, NASA/TM—2013-217822/PART1, 2013.

Pineda, E. J., Myers, D. E., Kosareo, D. N., Zalewski, B. F., Dixon, G. D., Buckling testing and analysis of honeycomb sandwich panel arc segments of a full-scale faring barrel – Part 2: 6-ply in-autoclave facesheets, NASA/TM—2013-217822/PART2, 2013.

Singer, J., Arboz, J., T. Weller, Buckling Experimental Methods in Buckling Thin Walled Structures, Basic Concepts, Columns, Beams and Plates – Volume 1, John Wiley & Sons, Inc., New York, 1998.

Schultz, M. R., Nemeth, M. P., Buckling imperfection sensitivity of axially compressed orthotropic cylinders, 51st AIAA/ASME/ASCE/AHS/ASC Structures, Structural Dynamics, and Materials Conference, 12-15 Apr., Orlando, FL, 2010.

Vinson, J. R., The Behavior of Sandwich Structures of Isotropic and Composite Materials, Technomic Publishing Co., Lancaster, PA, 1999.

Zalewski, B. F., Dial, W. B., Bednarcyk, B. A., Methods for assessing honeycomb sandwich panel wrinkling failures. NASA/TM—2012-217697, 2012.